9-2019

TIRS-2 and Future Thermal Instrument Band Study and Stray Light Study

Nicholas Bitten

nrb5526@rit.edu

TIRS-2 and Future Thermal Instrument Band Study and Stray Light Study

by

Nicholas Bitten

B.S, Physics, Rochester Institute of Technology

A thesis submitted in partial fulfillment of the
requirements for the degree of Master of Science
in the Chester F. Carlson Center for Imaging Science
Rochester Institute of Technology

September, 2019

Signature of the Author _____

Accepted by _____
    Coordinator, M.S. Degree Program   Date

CHESTER F. CARLSON CENTER FOR IMAGING SCIENCE

ROCHESTER INSTITUTE OF TECHNOLOGY

ROCHESTER, NEW YORK

<u>CERTIFICATE OF APPROVAL</u>

M.S. DEGREE THESIS

The M.S. Degree Thesis of Nicholas Bitten
has been examined and approved by the
thesis committee as satisfactory for the
thesis required for the
M.S. degree in Imaging Science

_____

Dr. Aaron Gerace, Thesis Advisor

_____

Dr. Carl Salvaggio

_____

Tania Kleynhans

_____

Date

THESIS RELEASE PERMISSION

ROCHESTER INSTITUTE OF TECHNOLOGY

CHESTER F. CARLSON CENTER FOR IMAGING SCIENCE

Title of Thesis:

**TIRS-2 and Future Thermal Instrument Band Study and Stray
Light Study**

I, Nicholas Bitten, hereby grant permission to Wallace Memorial Library of R.I.T. to reproduce my thesis in whole or in part. Any reproduction will not be for commercial use or profit.

Signature _____

Date

Acknowledgments

TIRS-2 and Future Thermal Instrument Band Study and Stray Light Study

Nicholas Bitten, M.S.

Rochester Institute of Technology, 2019

Supervisor: Aaron Gerace, Phd.

Abstract

Landsat thermal instruments have been a significant source of data for thermal remote sensing applications, and future Landsat missions will continue this tradition.

This work was designed to help inform the requirements for several parameters of future Landsat thermal instruments, and assess the impact that these parameters can have on the retrieved Land Surface Temperature (LST). Two main studies were conducted in this research. The first will investigate the impact that uncertainty in the spectral response of the bands will have on the LST product using the Split Window Algorithm. The main parameters that will be tested are the center and width of he bands. The second study will investigate the impact of stray light on LST, including different magnitudes of stray light and different combinations of in-field and out-of-field targets.

The results of the band study showed that shifting of the bands seems to be have a larger impact on the LST than widening of the bands. Small shifts of only +/- 50 nm can cause errors of over 1 K in the LST. This study also showed that atmospheres with more water vapor content will have more effected than those with lower water vapor.

The stray light study showed that using the stray light coefficients from TIRS-2 will not have a significant impact, when compared to the residual errors associated with the Split Window Algorithm.

Table of Contents

List of Tables

List of Figures

Chapter 1

Introduction

The Landsat series of satellites represent of the longest running sources of continuous satellite imagery, with Landsat-1 launching on June 23, 1972 [5] and Landsat-8, the most recent satellite, launching on February 11, 2013 [6]. Landsat-8 carries two instruments, the Operational Land Imager (OLI) and the Thermal Infrared Sensor (TIRS). Landsat-9 is now scheduled to launch in 2021 [7], and will be nearly a replica of Landsat-8. It will carry two instruments, the Operational Land Imager 2 (OLI-2) and the Thermal Infrared Sensor 2 (TIRS-2). Landsat-9 is a joint project between United States Geological Survey (USGS) and National Aeronautics and Space Administration (NASA), and will keep the Landsat legacy going.

The data collected from the Landsat series of satellites have been used in many applications, including agriculture, monitoring water usage, climate change, and land usage and monitoring [8]. It is important that the data collected by these satellites are as accurate as possible, so requirements for the individual parameters for the instruments need to be as refined and informed as possible.

1.1 Objectives

In order to ensure that the data collected by a satellite are accurate and usable, requirements are set for various aspects of the instruments. The goal of this thesis is to inform the requirements for future Landsat thermal instruments. Two separate studies were performed to evaluate the potential impact of several instrument design parameters on retrieved LST. The first study investigated the impact that alterations to the spectral bands can have on the retrieved LST. Parameters such as widening and shifting of the bands were investigated. The second study investigated the impact that stray light will have on the LST.

Three properties of the Relative Spectral Response (RSR) that will be looked into are the placement of the band centers, the width of the bands, and the general shape of the bands. The impact that these specific properties might have is not well known. Using TIRS-1 and TIRS-2 as references, the results of these studies will be used to inform requirements for future instruments.

Stray light will be a major concern for TIRS-2, as this is a known issue on TIRS-1. While the magnitude of the stray light has been reduced by about a factor of ten [9], the possible impact has not been researched in detail. The effects of stray light will be studied in detail with as many scenarios as possible, using preliminary measurements of the TIRS-2 stray light, as well as generalized stray light magnitudes to look at the impact from future instruments.

1.2 Layout of Thesis

The rest of this paper is organized as followed: Section 2 describes the relevant background for these studies, including thermal remote sensing topics and radiometry. Section 3 will discuss the data used for the studies, and the methods behind the different studies in this study. Section 4 discusses results from Split Window related studies. Section 5 discusses the results from the band study. Section 6 includes the results from the stray light study. Section 7 will be the summary and conclusion.

Chapter 2

Background

This section includes relevant background material that will be necessary to understand the rest of this paper. The first part of this section will discuss the two methods used to estimate LST using thermal imagers that are used in this study, the Split Window Algorithm and the Single Channel Method.

2.1 Thermal Remote Sensing

Thermal imaging is used to monitor land surface temperature throughout the world, using satellite and airborne instruments. This information is used in many fields, such as climate and weather monitoring/predictions, agriculture, and monitoring water use [6] [10] [11].

For thermal remote sensing, the radiometry is slightly different than for optical/reflective remote sensing. The main sources of light comes from self-emitted radiation from either the target or the atmosphere, as opposed to sunlight that is reflected or scattered.

Thermal radiation from a blackbody is defined using the Planck equa-
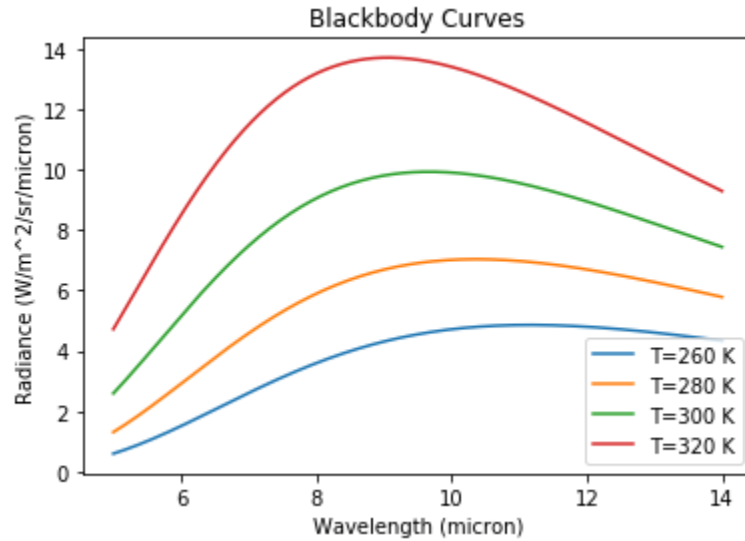
Figure 2.1: Plot of Blackbody curves in the thermal infrared at four temperatures.

tion, which is shown in Equation 2.1.

$$L_{T,\lambda} = \frac{2hc^2}{\lambda^5} \frac{1}{e^{\frac{hc}{\lambda kT}} - 1} \tag{2.1}$$

Where h is the Planck constant, c is the speed of light, λ is the wavelength in μm, k is the Boltzmann constant, and T is the temperature of the object. The thermal radiance, $L_{T,\lambda}$ is measured in $\frac{W}{m^2 sr \mu m}$.

Figure 2.1 shows a plot of the Planck equation at different temperatures. It is clear that there is a wide range in the magnitude of the blackbody curve, as well as the peak wavelength of the curve.

2.1.1 Radiative Transfer Equation

This section will cover the Radiative Transfer Equation (RTE), which describes the radiometry necessary for calculating the at-sensor radiance for a given instrument. The at-sensor radiance is the summation of all the possible paths that light can take to reach the detector, including reflected light, scattered light and thermal radiation. Figure 2.2 shows each of these paths.

Path A is the sunlight that is directly reflected off of the target. Path B is sunlight that is scattered in the atmosphere and is then reflected off of the target. Path C is light that is scattered in the atmosphere directly at the sensor. Path D is thermal radiation that is self emitted by the target. Path E is thermal radiation emitted by the atmosphere and is then reflected off of the target. Path F is thermal radiation emitted by the atmosphere directly at the sensor. Path G is light reflected off of some object, and then reflected off of the target back towards the detector. Path H is thermal radiation emitted by an object that is then reflected off of the target towards the detector.

The RTE is shown below in Equation 2.2:

$$L_{AS} = [E'_{s,\lambda}cos(\sigma')\tau_1(\lambda)\frac{r(\lambda)}{\pi} + \epsilon(\lambda)L_{T,\lambda} + F(E_{d,s,\lambda} + E_{d,\epsilon,\lambda})\frac{r(\lambda)}{\pi}$$

$$+ (1 - F)(L_{b,s,\lambda} + L_{b,\epsilon,\lambda})r_d(\lambda)]\tau_2(\lambda) + L_{u,s,\lambda} + L_{u,\epsilon,\lambda}$$

$$= L_A + L_D + L_B + L_E + L_G + L_H + L_C + L_F \quad (2.2)$$
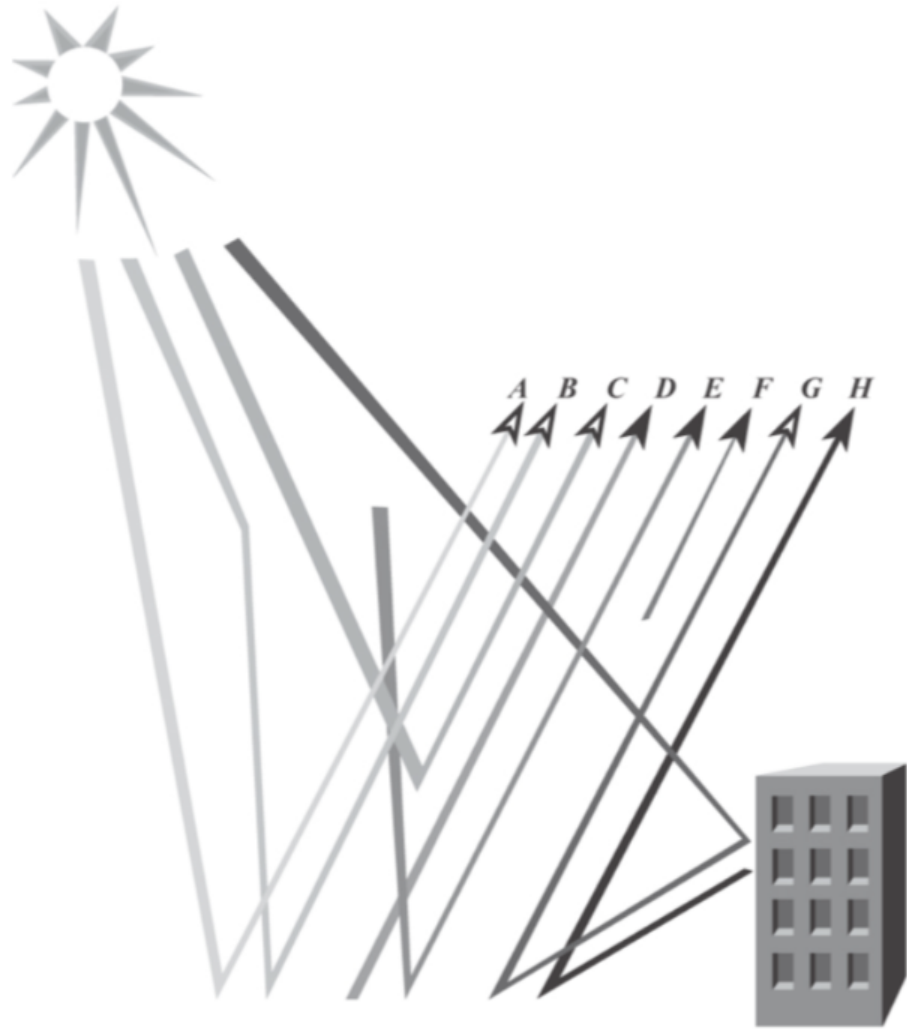
Figure 2.2: This figure shows the possible paths that light can take to reach the sensor. Path A: Direct reflected sunlight. Path B: Reflected scattered sunlight. Path C: Direct scattered sunlight. Path D: Self emitted light. Path E: Atmosphere emitted radiation reflected off of target. Path F: Atmospheric emitted radiation. Path G: Sunlight reflected off of object, reflected off of target. Path H: Self emitted radiation from an object. Figure is from [1]

Defining the variables in equation 2.2, τ_1 is the cumulative transmission of the atmosphere between the sun and the target, τ_2 is the cumulative transmission of the atmosphere between the target and the detector, ϵ is the emissivity of the target, r is the reflectance of the target, r_d is the reflectance of the building/object, σ' is the zenith angle of the sun, F is the fraction of the sky that is unobstructed by objects/buildings.

For the radiometric terms, $E'_{s,\lambda}$ is the spectral irradiance of the sun, $L_{T,\lambda}$ is the thermal emitting radiance of the atmosphere, $E_{d,s,\lambda}$ is the irradiance of the scattered sunlight that reaches the target, $E_{d,\epsilon,\lambda}$ is the self emitted irradiance of the atmosphere that reaches the target, $L_{b,s,\lambda}$ is the radiance of sunlight that reflects off of the building, $L_{b,\epsilon,\lambda}$ is the self emitted radiance of the building, $L_{u,s,\lambda}$ is the sunlight that is scattered up towards the detector, and $L_{u,\epsilon,\lambda}$ is the self emitted radiance of the atmosphere that reaches the detector.

Since this study will be focused on thermal infrared measurements, Only thermal contributions will need to be considered. Any contributions from buildings will also be ignored, which leaves the following terms: L_D, L_E, and L_F. The at-sensor radiance is defined in Equation 2.3.

$$L_{AS} = [\epsilon(\lambda)L_{T,\lambda} + E_{d,\epsilon,\lambda}\frac{1 - \epsilon(\lambda)}{\pi}]\tau_2(\lambda) + L_{u,\epsilon,\lambda} \qquad (2.3)$$

L_D, L_E, and L_F are also called the Upwelling Radiance, Downwelling Radiance and Atmosphere Emitted Radiance, respectively.

2.1.2 Split Window Algorithm

The Split Window algorithm is used to estimate the LST of a target using the apparent temperature from two Thermal IR channels. The advantage of the split window algorithm is that it can compensate for atmospheric effects without using reanalysis data, making it easier to use than the Single Channel Method, which is described below. Previous thermal instruments on Landsat missions only had a single channel, and TIRS was designed with two bands specifically to use the split window algorithm. Because of this, the Split Window Algorithm will be the primary method used for LST calculations in this paper.

The Split Window Algorithm is used to estimate LST on several space-borne thermal imagers, such as MODIS and AVHRR [12] [13].

The Split Window algorithm only requires four inputs, the brightness temperature and emissivity at each of the two bands. The equation used in this method was originally developed for MODIS [13], but was refined for Landsat 8 in du et al 2015 [14], and is described below:

$$LST = b_0 + (b_1 + b_2 \frac{1-\epsilon}{\epsilon} + b_3 \frac{\Delta\epsilon}{\epsilon^2}) \frac{T_{10} + T_{11}}{2} + (b_4 + b_5 \frac{1-\epsilon}{\epsilon} + b_6 \frac{\Delta\epsilon}{\epsilon^2}) \frac{T_{10} - T_{11}}{2} + b_7 (T_{10} - T_{11})^2$$

$$(2.4)$$

The two temperatures, T_{10} and T_{11}, are the brightness temperatures at the two bands, ϵ is the average of the emissivity at the two bands, and $\Delta\epsilon$ is

the difference between the emissivity at the two bands. The b-coefficients are found using simulations, and this process will be described in Section 3.

2.1.3 Single Channel Method

The Single Channel Method uses the signal from a single thermal band to estimate the LST. Instead of a statistical approximation (ie. the Split Window Algorithm), this method uses the RTE to solve for the temperature of the target. Equation 2.3 is solved for $L_{T,\lambda}$ in order to calculate the self-emitted radiance of the target, which is then converted to surface temperature using the inverse Planck Equation. The former equation is shown below:

$$L_{T,\lambda} = [(L_{AS} - L_{u,\epsilon,\lambda})\frac{1}{\tau_2(\lambda)} - E_{d,\epsilon,\lambda}\frac{1 - \epsilon(\lambda)}{\pi}]\frac{1}{\epsilon} \qquad (2.5)$$

And the inverse Planck equation is shown here:

$$T = \frac{hc}{\lambda k}\frac{1}{ln(\frac{\lambda^5}{2hc^2 L_{T,\lambda}} + 1)} \qquad (2.6)$$

In order to solve this equation, atmospheric terms are estimated using reanalysis data, as well as forward modeling using MODTRAN. Simply put, reanalysis data takes measurements of multiple atmospheric parameters, and interpolates them in the space between the measurements. Instead of reanalysis data, radiosonde measurements can also be used. Radiosondes are weather balloons that record multiple atmospheric parameters, such as tem-

perature, pressure and humidity as a function of altitude as the balloon rises. Radiosonde collections are the best source of atmospheric profiles, but the locations where they are collected are separated by large distances, with only 69 sites located in the lower 48 states. The radiosondes are launched at 0000 and 1200 UTC, which corresponds to 8:00 PM and 8:00 AM EST. These large distances and relatively low temporal resolution raise a concern about using these measurements for locations that are significantly far away, and at times hours from the collections. However, the reanalysis data uses ground and satellite measurements, as well as meteorological models, to estimate the parameters in between the measurements. More in depth information can be found in Rienecker et al 2011 [15], which describes the Modern-Era Retrospective Analysis for Research and Applications (MERRA), a common reanalysis product developed by NASA.

The Single Channel Method is commonly used to estimate LST using TIRS-1, using each of the two thermal bands separately [16].

2.2 TIRS Instrument Overview

2.2.1 Instrument Design

TIRS-2 is essentially a copy of TIRS-1, with a few updates to improve the performance, most notably to reduce the stray light impact. Landsat-9 is still being characterized and measured, so there are no available measurements of the RSR's of the two bands. I will have to use the measurements from TIRS-

11

Table 2.1: Comparison of the measured and required NEdL for the two bands at different source temperatures. All values are in $W/m^2/sr/\mu m$. *Values at 240 K are taken from pre-flight measurements.

Source Temperature (K)	Band 10		Band 11	
	Measured	Requirement	Measured	Requirement
240*	0.0054	0.059	0.0053	0.049
270	0.0062	0.059	0.0058	0.049
300	0.0070	0.059	0.0064	0.049
320	0.0075	0.059	0.0072	0.049

1 for the time being.

TIRS-1 is a push broom instrument with three focal plane arrays and two bands, as shown in figure 2.3. A push broom sensor contains a single linear array of detectors per band, and as the instrument moves over the ground, it collects a time series of these one-dimensional images, which can be converted into a two-dimensional array.

TIRS-1 contains two bands, Band 10 centered at 10.9 μm, and Band 11 centered at 12.0 μm. These two bands were chosen due to their position in the atmospheric transmission window, a region between 10 and 14 μm where the atmosphere allows most of the thermal radiation through. The bands also overlap with the single thermal band of Landsat 7.

The Ground Sample Distance (GSD) is 100 m, which is over three times more than the 30 m GSD of the OLI instrument.

(a)

(b)

(c)
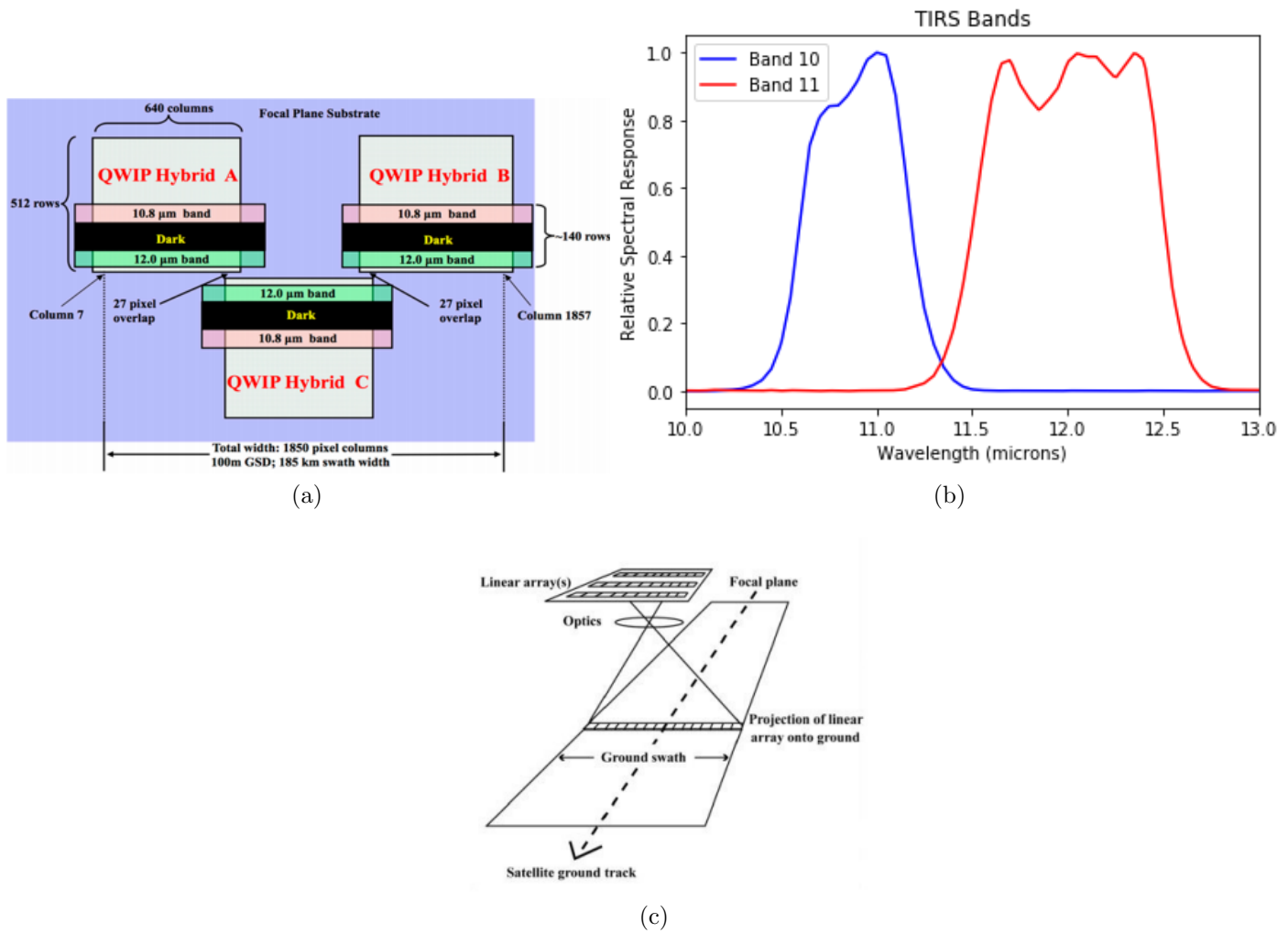
Figure 2.3: Figure (a) shows the focal plane array of TIRS-1 [2]. The three focal plane arrays each have three bands, including the two thermal bands and a dark band used to measure the dark current. Figure (b) shows the spectral response of the two thermal bands of TIRS-1 [2]. Figure (c) shows how the general operation of a push broom sensor [3].

Table 2.2: Comparison of the measured and required NEdL for the two bands at different source temperatures. All values are in $W/m^2/sr/\mu m$. *Values at 240 K are taken from pre-flight measurements.

Source Temperature (K)	Band 10		Band 11	
	Measured	Requirement	Measured	Requirement
240	0.074	0.80	0.078	0.71
270	0.057	0.56	0.060	0.53
300	0.049	0.40	0.052	0.40
320	0.045	0.35	0.051	0.35

2.2.2 Instrument Performance

The TIRS instrument has demonstrated very good on-orbit performance. Table 2.1 shows the required and measured NEdL, and Table 2.2 shows the required and measured NEdT [17]. The performance is much better than the requirements by about a factor of ten in every case. In comparison, the thermal band on Landsat 7 had an NEdL of 0.115 $W/m^2/sr/\mu m$ and an NEdT 0.45 K [18], so TIRS-1 is a significant improvement over the Landsat 7 thermal imager.

2.3 Stray Light and TIRS

Stray Light can be characterized as light outside the field-of-view of a detector that causes an additional signal. This typically is the result of light reflecting/refracting or emitting off of parts of the instrument. Stray light results in calibration errors that can be difficult to correct for, since the signal is out-of-field and therefore unknown.
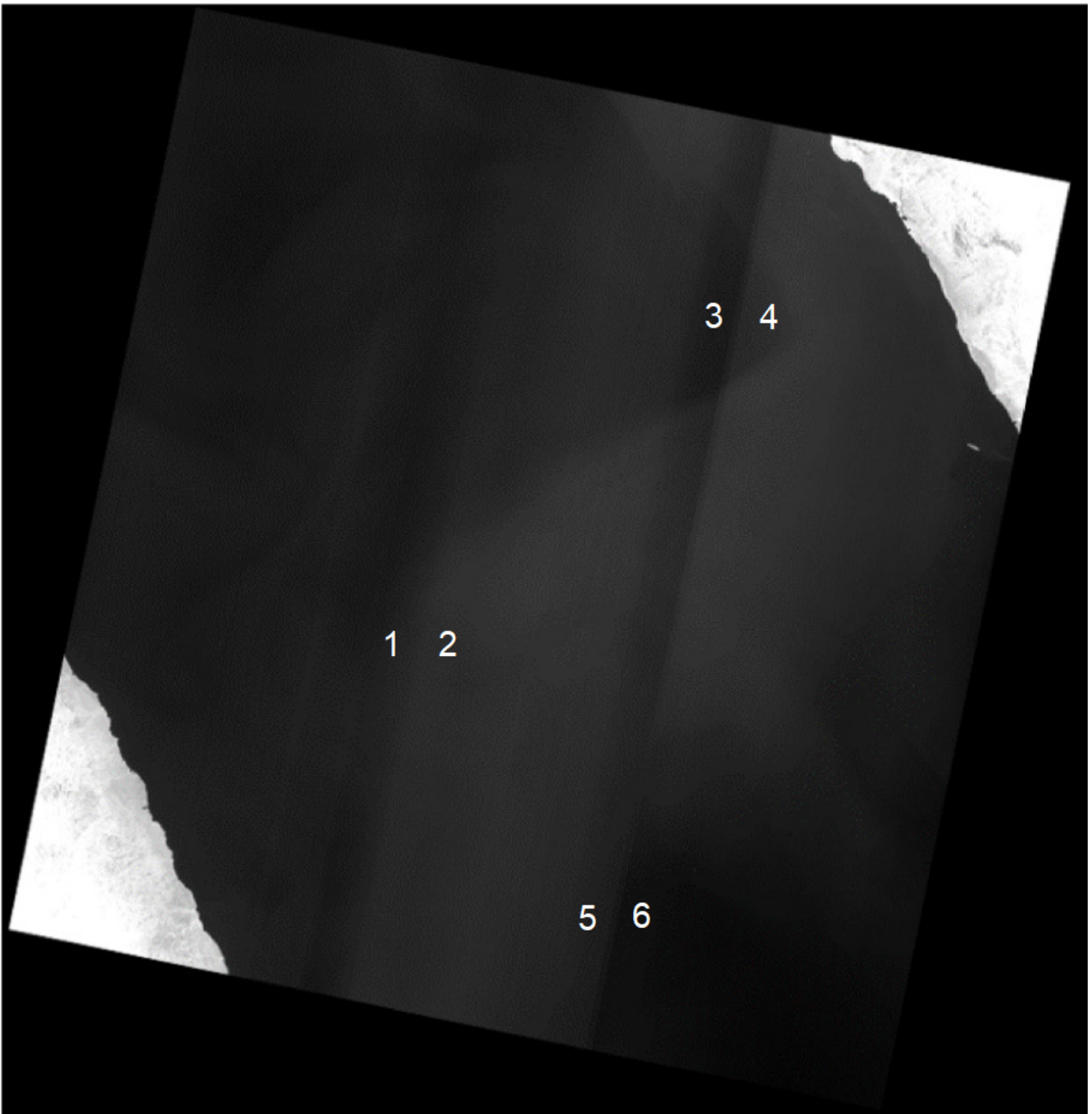
Figure 2.4: This figure shows an example of stray light in a TIRS Band 11 radiance image of the Red Sea with significant stray light signal. Several points of interest are labeled by number. This figure is taken from Montanaro et al 2014 [4].

An example of stray light artifacts are shown in Figure 2.4 [4]. The Red Sea is surrounded by much hotter land, which makes it an ideal location to demonstrate the impact of stray light. There is a noticeable difference between the different focal plane arrays, which is most prominent at the borders between them, such as between points 1 and 2, 3 and 4, and 5 and 6 on Figure 2.4. It is important to notice that the banding effect is not uniform to the along track direction, which is obvious when looking between points 3 and 5, where the signal increases in a way that is unexpected if there was a simple streaking effect due to the detectors uniformity.

2.4 Background Summary

This chapter serves to describe the relevant background material needed to understand the different methods used to calculate LST with satellite based thermal imagers, and the relevant radiometry behind them. Throughout the rest of this paper, the Split Window Algorithm will be the primary method used to estimate LST. The RTE describes how radiation propagates through the atmosphere, including different atmospheric contributions such as transmission and up-welling radiance.

Chapter 3

Methods and Data

This chapter will describe the data that will be used to perform the two main studies, and the methods in which they will be performed. The two sources of data that are used are the TIGR atmospheric dataset and the ASTER spectral emissivity dataset. The Split Window section will describe how the split window coefficients are generated, how LST is calculated using this algorithm, and how errors will be propagated through Equation 2.4.

The methods used for the band trade study will be described in Section 3.4, which will describe how the bands will be altered, and how the impact of altering certain parameters of the bands will be measured.

The methods for the stray light study will describe how stray light signals will be included in simulated measurements, and how the impact it will have on LST will be measured.

3.1 TIGR Atmospheric Data

The atmospheric profiles used throughout this study come from the Thermal Initial Guess Retrieval (TIGR) dataset [19] [20] [21]. This dataset

17

contains 2311 unique atmospheric profiles from radiosonde collections.

This dataset is part of an effort to segment over 80,000 radiosonde collections into unique atmospheres. They used statistical methods to separate these into unique profiles out of all of these collections, and they end up with 2311 atmospheres. The dataset is split into 872 tropical atmospheres, 387 mid-latitude-1 atmospheres, 353 mid-latitude-2 atmospheres, 103 polar-1 atmospheres, and 392 polar-2 atmospheres.

3.2   Spectral Emissivity Data

In this study, 113 high spectral resolution emissivities are used, with 546 data points between 8 and 14 μm for each emissivity [22]. These emissivity spectra consist of 74 soil/minerals, 26 vegetation, and 13 water/ice emissivities, in order to cover a variety of naturally occurring materials. Man made materials are not included in this study due to the low spatial resolution of Landsat thermal instruments, as most man made materials are too small to take up an entire Landsat pixel. Pixels with only a single emissivity will be considered, mixed pixels will not be used in this study.

3.3   Split Window Procedure

This section will explain the procedure used to derive the coefficients used for the split window algorithm, as shown in Equation 2.4. The coefficients are found using simulated data, based off of measured atmospheric profiles and

emissivities described in Sections in 3.1 and 3.2. In order to get coefficients that can be used globally, the simulations need to contain as much variation as possible. This is why the 2311 TIGR atmospheres and 113 spectral emissivities are used. For most Split Window Algorithms, the temperatures used are -10 K to + 20 K of the temperature of the lowest layer of the atmosphere, with increments of 5 K [14]. This results in 1,828,001 different scenarios that are used in this study. MODTRAN is used to calculate spectral radiance for each of these scenarios, which are then sampled by the bands for TIRS to generate band-effective-radiance values. The procedure used for this is detailed below:

Step 1: Run MODTRAN for 2311 TIGR atmospheric profiles. This generates downwelling irradiance, atmospheric emitted radiance and atmospheric transmission for each atmosphere.

Step 2: Calculate surface-emitted radiance for 7 temperatures and 113 emissivities.

Step 3: Calculate Downwelling radiance, for 113 emissivities per atmosphere.

Step 4: Calculate the Band Effective radiance and Band Effective Emissivity at the two TIRS bands for every at-sensor Spectral Radiance Curve.

Step 5: Convert to brightness temperature using inverse Planck equation.

Step 6: Fit Split Window equation to brightness temperatures and

emissivities.

In addition to simply using all of the atmospheres there are several ways to reduce the LST error in the Split Window process by only using a select few atmospheres. The first reduction is to only use atmospheres with a relative humidity that is less than 90%, as these atmospheres most likely are very cloudy and thus would not be used in any real scenarios in the first place. On top of that, one can calculate coefficients using different values of CWV. In Du et al [14] they split the atmospheres into five separate CWV ranges, 0.0-2.5 g/cm^2, 2.0-3.5 g/cm^2, 3.0-4.5 g/cm^2, 4.0-5.5 g/cm^2, and 5.0+ g/cm^2. By separating the atmospheres into different categories, the coefficients generated are able to compensate for different atmospheric features due to different levels of water vapor in the atmosphere. This will be shown in more detail later in this paper.

3.3.1 Split Window Sensitivity Analysis

This paper will look at the impact that various errors will have on the predicted LST using the Split Window Algorithm. The goal of this section is to look at how sensitive the Split Window Algorithm is to bias in the measured at-sensor radiance and brightness temperature. The Split Window Algorithm relies on the calculated coefficients to estimate the LST, but it is not readily apparent how the equation is dependent on the individual inputs. This will be important to understand how sensitive the Split Window equation is to error

in different parameters, which will help explain the results from the studies later on in this paper.

This will be done by simply increasing the signal of each band by separate amounts, and comparing the result to the nominal signal. This is shown in the equation below:

$$\Delta LST = LST(T'_{10}, T'_{11}) - LST(T_{10}, T_{11}) \tag{3.1}$$

T'_{10}, T'_{11}, T'_{10} and T'_{11} are defined as:

$$T_{10} = T(L_{10}), T_{11} = T(L_{11})$$
$$T'_{10} = T(L_{10} + \delta L_{10}), T'_{11} = T(L_{11} + \delta L_{11}) \tag{3.2}$$

Where $T(L)$ is the brightness temperature of a given radiance value, as defined in the inverse Planck equation (Eq. 2.6). The extra signal/error δL_i will be a fraction of the nominal signal, to see how this will effect the LST. The difference between the LST predicted with and without this radiance error is ΔLST.

This is essentially a generalization of stray light, and will give an idea of how stray light of different magnitudes in each of the bands can have varying effects on the LST.

3.4 Band Study Methods

One of the main objectives of this project is to determine the impact of uncertainty in measured spectral response on retrieved LST. This study may be

used to help inform the requirements for future thermal instruments. The main parameters that are investigated here are the center of the bands, the width of the bands, and the uniformity of the bands, which is the variation between the response of the individual detectors. This may become a significant problem when the actual bands are significantly different than they were measured in the lab, which means they will sample at-sensor radiance differently than expected.

In order to test these properties, scenarios need to be recreated where a certain RSR is assumed, but the at-sensor radiance of a target is sampled using a different RSR. The procedure to do this involves deriving the split window coefficients using the nominal bands, and then using these coefficients to predict LST for radiance sampled using a test set of RSR's. Small variations in the RSR will cause changes in the retrieved radiance, impacting the retrieved LST.

3.4.1 Band Shifting and Widening

Consider Figure 3.1, which shows the location of the two TIRS-1 bands relative to the at-sensor radiance curve associated with a target at three different surface temperatures that has been propagated through a MLW atmosphere. It is clear that there are many absorption or emission features near the bands, most notably near the right edge of Band 11 for the target with a temperature of 290 K. It is obvious that the surface temperature has a significant
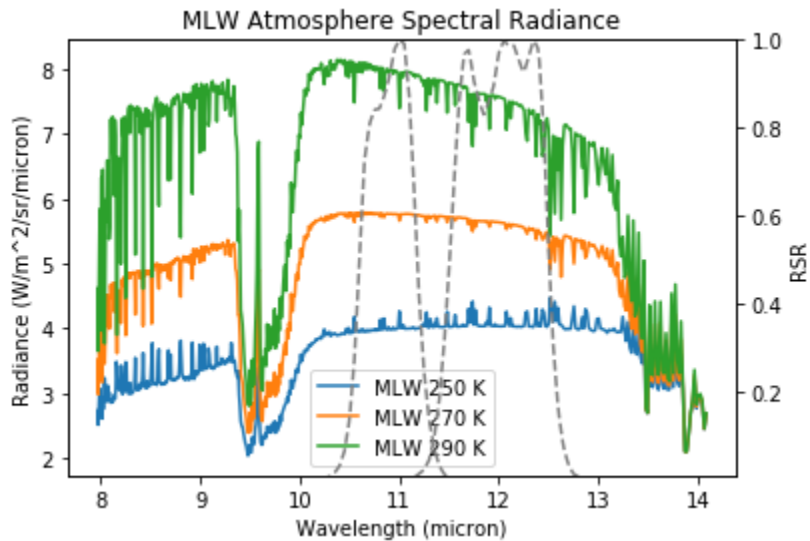
Figure 3.1: This figure shows the location of the bands relative to the spectral radiance for several surface temperatures.

effect on the shape of the spectra, which makes sense when looking at Figure 2.1, where the peak of the blackbody curve shifts towards higher wavelengths and the magnitude decreases. The features will also be different with different atmospheres, as the water content can cause the water absorption features to be more significant. As the two bands are shifted or widened as suggested in this study, they will sample different parts of the spectra, which will make the target appear hotter or colder than it really is.

3.4.2 Band Shape

This section will look at how the shape of the bands can affect the retrieved LST. This will be done in several different ways, including switching

the shape of bands 10 and 11 with each other, replacing the bands with gaussian bands and rectangular bands, and generally adjusting the shape of the bands.

The first part of this will be replacing the shape of the two bands with each other. What this means is that the shape of Band 10 will be copied and will replace the shape of Band 11 in the same location as Band 11, and this will also be done with the shape of Band 11 replacing Band 10, and then switching the shape of the bands. These bands are shown in Figure 3.2. This will be done in order to look at how the shape of the bands vs the location of the bands effects the LST. The same procedure for the shifting and widening of the bands will be repeated for these different scenarios.

The next study will be looking at how Gaussian or rectangular bands respond to shifting and widening. These two band shapes are idealized versions of a spectral response, and Band 10 is similar to a Gaussian shape, and Band 11 is similar to a rectangular band.

In addition to looking at how the rectangular and Gaussian bands are effected by shifting and widening, the general shape of the bands also should be investigated. This is done since each individual detector will have their own response that will vary from the average RSR. In order to alter the bands, the nominal bands are combined with the rectangular and Gaussian bands. What this means is that the bands will be some fraction of the nominal bands and the rectangular or Gaussian bands. In equation form, this can be expressed

24
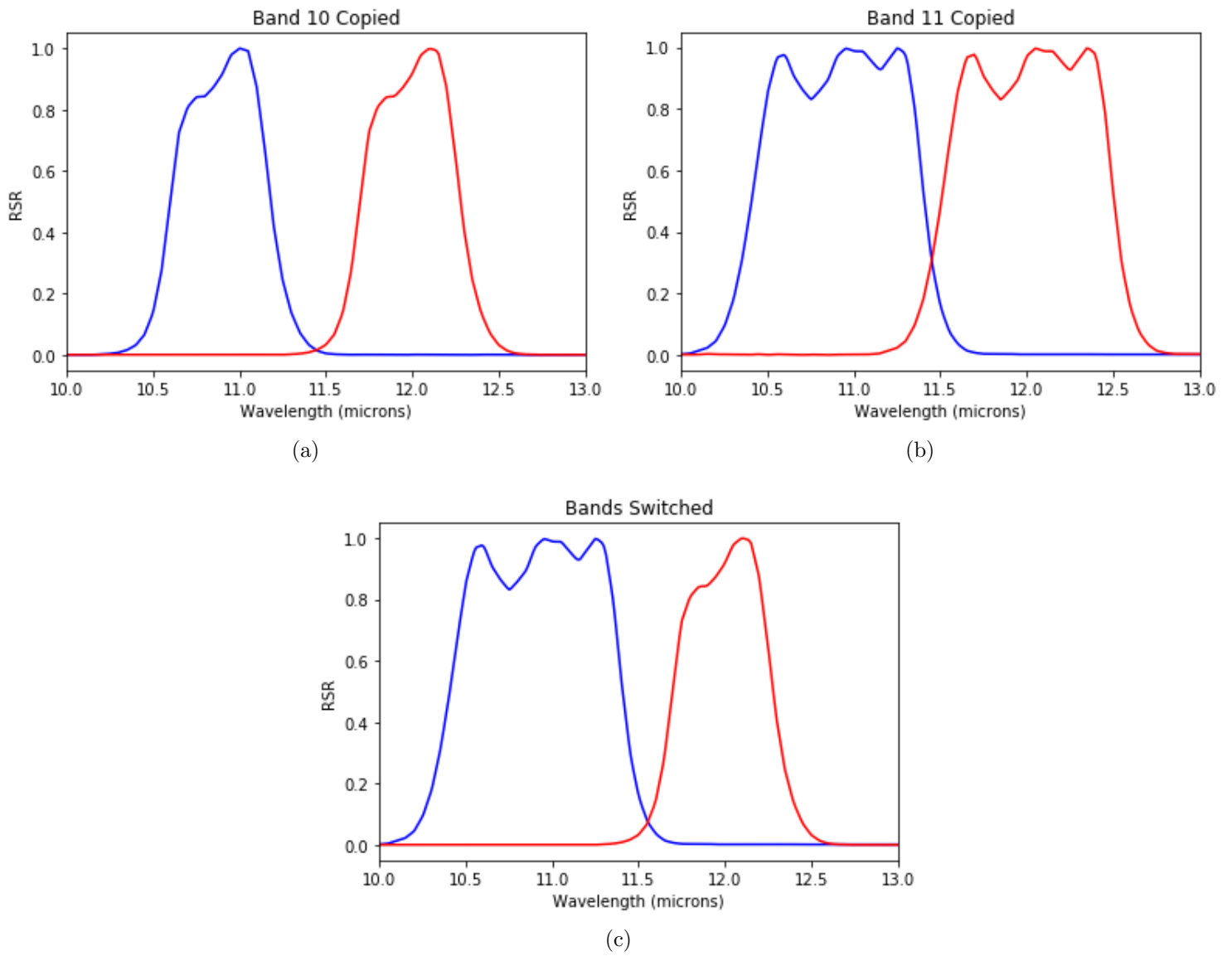
Figure 3.2: Showing the shapes of the bands being copied or switched.
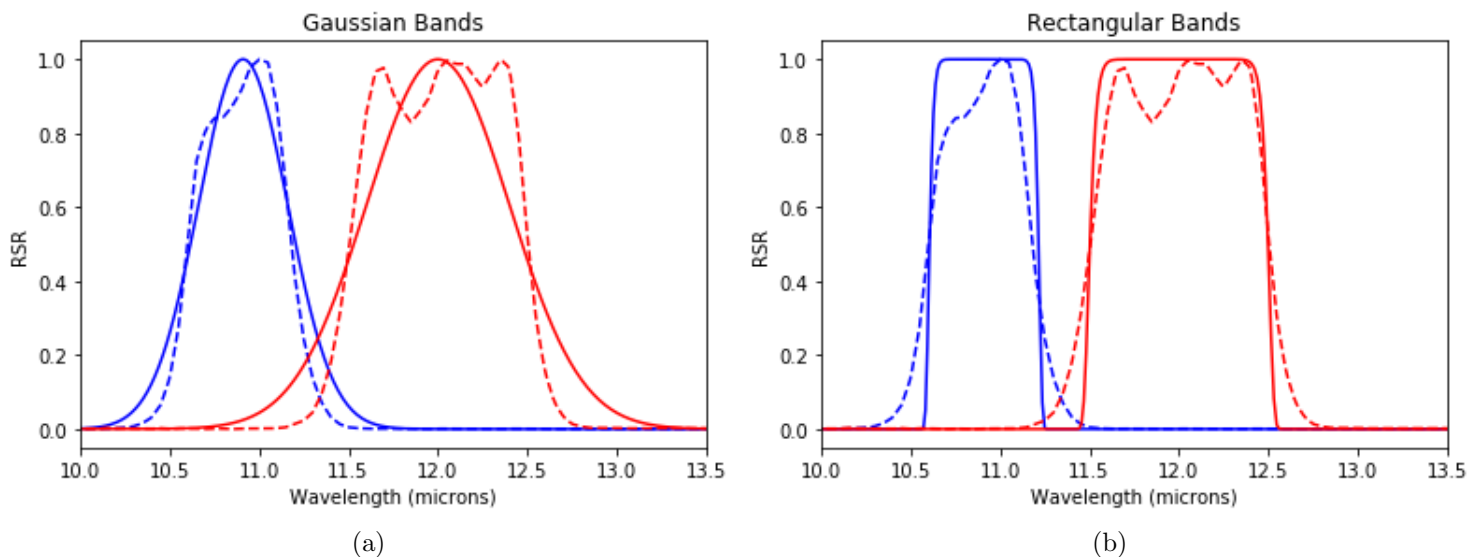
Figure 3.3: Showing the shapes of the Gaussian and rectangular bands with the same center and width of the nominal bands.

as: $RSR = fRSR_{nom} + (1 - f)RSR_{gauss}$, where f is the fraction that is the nominal bands vs the ideal band. This will give some unique band shapes that may produce some interesting results. These band shapes are shown in Figure 3.4, as the solid-lined curves, while the dashed-line curves show the nominal bands and the gaussian/rectangular bands.

3.5 Stray Light Analysis

In this study, a simplified model of stray light will be used in order to determine the possible impact that it may have on the retrieved LST. In this model of stray light, geometric properties won't be considered, but instead the
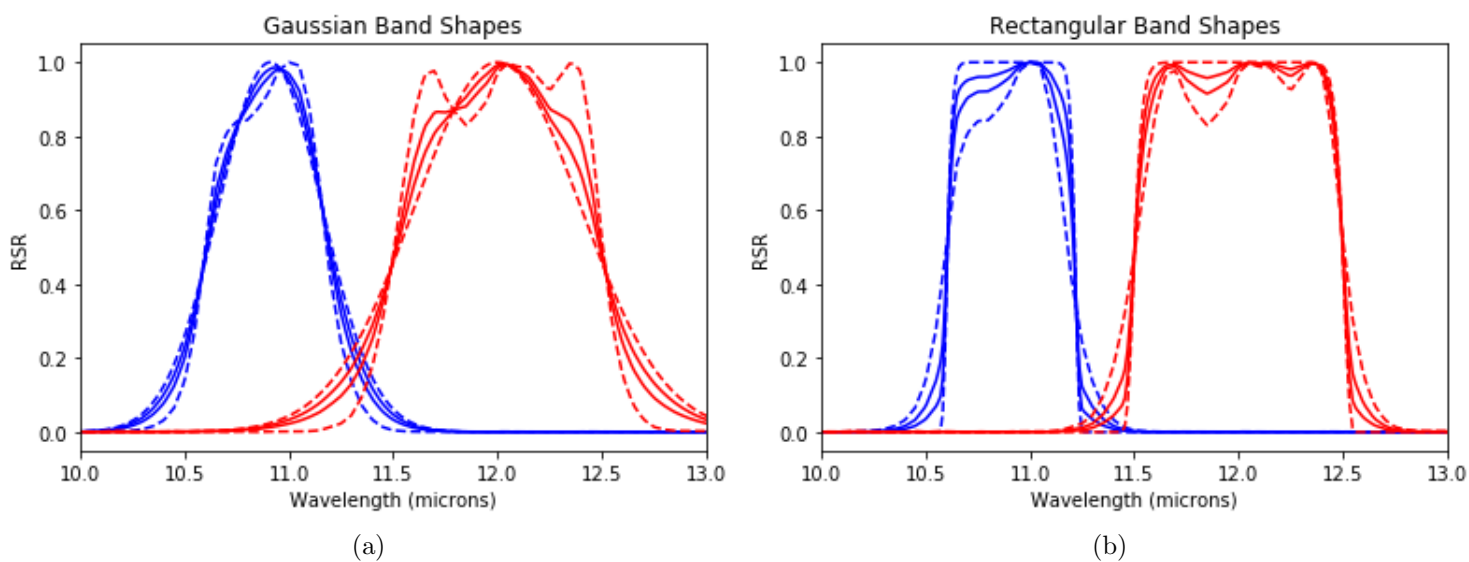
Figure 3.4: This figure shows the bands that are combinations of the nominal bands and Gaussian bands. The dotted lines are the nominal and Gaussian/rectangular bands, and the solid lines are the combination of the two, the two values shown are 50% nominal and 25% nominal.

Figure 3.5: A visualisation of the simplified stray light model used for this study.

entire field of view will contain a single in-field target with a given emissivity and temperature, and an out-of-field target with another emissivity and temperature will be the source of stray light. Figure 3.5 shows an example of a simplified target.

The amount of stray light will vary with each detector, and values that will be used for TIRS-2 will come from preliminary measurements of stray light testing. There are two main sources of stray light, coming from 13 and 22 degrees out of field, and each of these fall on different areas of the focal plane array.

Stray light will be incorporated into at-sensor radiance according to:

$$L_{total} = L_{IF} + f_{SL}L_{OOF}$$

Where L_{IF} is the at-sensor radiance of the in-field target, L_{OOF} is

the at-sensor radiance originating from the out-of-field target, and f_{SL} is the fraction of the out-of-field signal that is added to the total signal.

3.5.1 Stray Light Procedure

In this section the procedure used to measure the impact of stray light on LST is described. Each scenario simulated here will include an in-field target with a given temperature, an out-of-field target with a separate temperature, and atmospheric conditions for each scenario.

Step 1: Obtain nominal split window coefficients as described above in Section 3.3.

Step 2: Calculate spectral radiance for the in-field scenario.

Step 3: Calculate spectral radiance for the out-of-field scenario.

Step 4: Calculate the stray light signal using $L_{total} = L_{IF} + f_{SL}L_{OOF}$ for each band.

Step 5: Calculate the band effective radiance at each band, with and without stray light, and convert to brightness temperature.

Step 6: Use the two brightness temperatures to calculate the LST using the split window coefficients, for the stray light and no stray light cases.

Step 7: Compare the retrieved LST values with and without stray light.
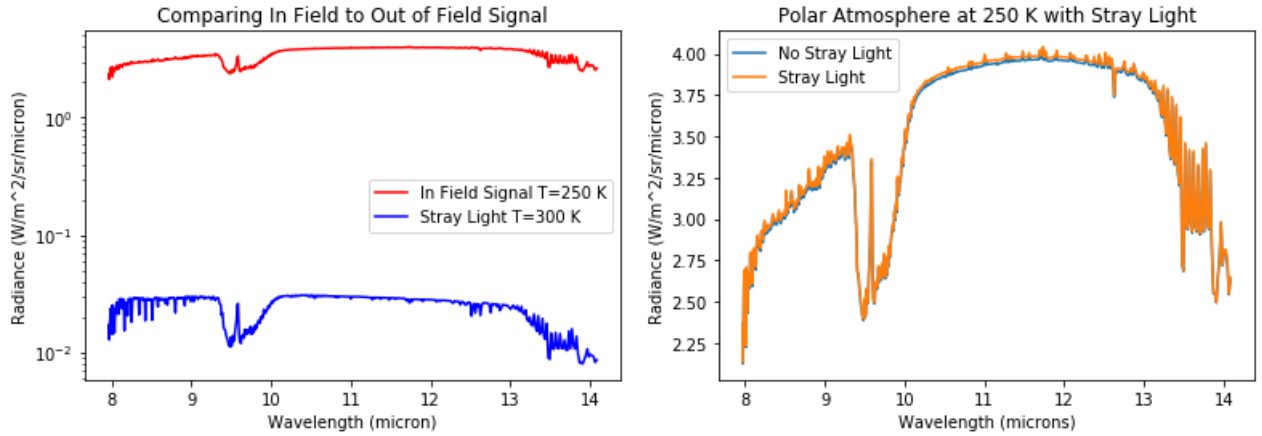
(a) Comparing IF signal to OOF Signal. (b) Comparing a signal with and without stray light.

Figure 3.6: This figure is to compare the signal of Stray Light to the nominal signal. In this figure, the in-field temp is 250 K, and the out-of-field temp is 300 K. Figure a. shows the relative magnitudes of the in-field and out-of-field signals on a Logarithmic scale. The out-of-field signal is orders of magnitude smaller than the in-field. Figure b. shows how close the signal is with and without stray light.

3.5.2 Emissivity Contribution

This section will look at how having different materials in-field and out-of-field can affect the retrieved LST. Having a different emissivity in-field and out-of-field will be more realistic than the previous study that simply used blackbodies. Using the 113 emissivities described in Section 3.2, there will be 113*113 (12,769) emissivity combinations for each temperature combination and atmosphere.

3.5.3   Single Channel Method

In addition to using the Split Window Algorithm, the Single Channel Method should also be considered, as it is a commonly used technique to calculate LST for single band thermal instruments. This method assumes all quantities can be estimated to solve the RTE, so any additional signal will cause an error in the LST. The Single Channel Method will use the equations as described in Section 2.1.3, and the stray light will be added to the at-sensor radiance as described in the Section 3.5.1.

3.6   Informing Requirements

As stated earlier, the main point of this project is not to simply look at the impact that the spectral response or stray light may have on LST, but to use the results to potentially inform requirements for future Landsat thermal instruments. In order to do this, the resulting error in LST will be compared to the noise of the system, in order to determine if the LST error will be large enough to potentially effect higher level products.

Chapter 4

Split Window Results

This section will include the results of various preliminary Split Window studies that will be used to calculate the Split Window Coefficients and to help understand the accuracy of the Split Window Equation, and the sensitivity to different sources of error.

This section will focus on results using the Split Window Algorithm. The coefficients used for the Split Window Algorithm are calculated, and the accuracy of the LST retrieval is analyzed. The description of how and why these studies are performed are described in Section 3.3. These preliminary studies will be used to put the results of the two main studies into context.

4.1 Split Window Coefficients

The Split Window coefficients from Equation 2.4 were calculated for five different conditions. The first simply uses all of the atmospheres with no discrimination. The next condition is to only consider atmospheres with a relative humidity less than 90%. The remaining conditions is splitting the previous atmospheres into three different categories based off of column water

Table 4.1: Table of Split Window Coefficients

	Conditions	Percent of All Atmospheres	b0	b1	b2	b3	b4	b5	b6	b7	RMS Error (K)
1.	All Atmospheres	100	2.01	0.99	0.14	-0.34	4.44	-0.82	5.75	0.19	1.02
2.	Rel Humidity less than 90%	60	1.80	1.00	0.15	-0.31	3.69	0.81	-3.02	0.17	0.71
2.	Limit CWV from 0.0-2.5	52.44	-0.52	1.00	0.16	-0.33	3.72	6.33	-0.63	0.04	0.34
3.	Limit CWV from 2.5-4.0	6.18	5.57	0.98	0.12	-0.17	6.28	6.78	-14.13	-0.02	0.61
4.	CWV Greater than 4.0	1.47	-5.94	1.00	0.07	-0.06	9.20	8.34	-14.33	-0.11	1.02

vapor values: 0-2.5 g/cm^2, 2.5-4 g/cm^2, 4+ g/cm^2. Each of the different conditions resulted in different sets of split window coefficients, with different RMS errors. These results are shown in table 4.1, with the eight coefficients, the percent of atmospheres contained in each of the conditions, and the RMS error (of the simulated data) of each of these conditions in the last column. Comparing the results from simply using all of the atmospheres to limiting the Column Water Vapor (CWV) values shows that it is very beneficial to do this. The obvious advantage to using all of the atmospheres is that no prior knowledge of the CWV required, but a basic estimation could result in significantly reduced errors.

For this effort, CWV will be ignored and the coefficients found using less than 90% relative humidity will be used. Out of the original 1,828,001 scenarios, this leaves 1,098,699. The RMS error of 0.71 K is relatively small
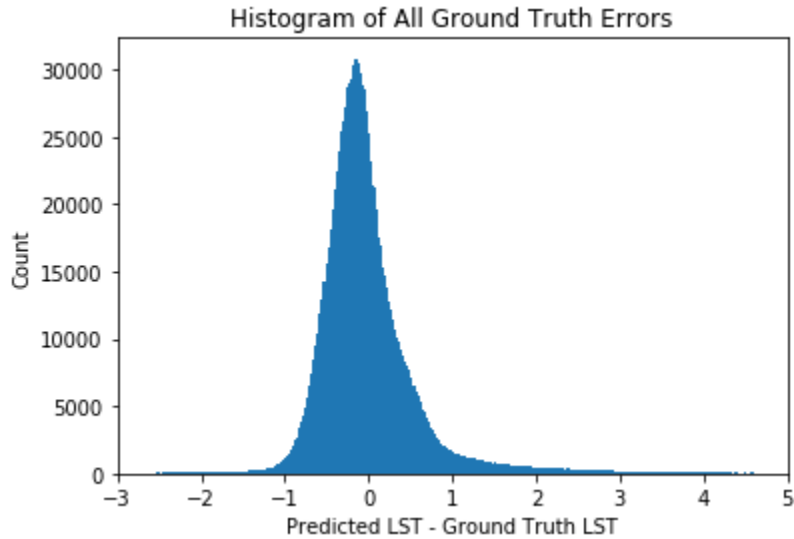
Figure 4.1: Histogram of ground truth error from the split window predicted LST using reduced humidity coefficients.

for such a large variety of targets. This error can be explored to get an idea for what the difference between the split window LST and ground truth surface temperature (actual LST) actually looks like for all of the simulated measurements. The distribution of errors is shown in Figure 4.1, and is nearly Gaussian with asymmetric tails. The tails are cut short in order to view the distribution better, but the max error is 15.5 K and the min is -8.9 K. Of course, most of the error is contained within $+/- 1$ K, with only 6.4 % having an error higher than this. Only 0.9 % have an error larger than 3 K. This is not necessarily negligible, but these extreme cases are still rare.

Delving more into the details of the LST error, certain parameters that may effect the retrieved LST are considered. The first one is the CWV of the

atmosphere. To assess the impact of CWV on the retrieved LST, the CWV values are split into bins, and the RMS error of the predicted vs. actual LST is calculated in each of the bins. The bins are chosen such that there are enough samples in each bin to get a good average, while still having enough bins to find a trend. This is shown in Figure 4.2. The obvious trend is that the error increases with CWV, which should be expected, as water vapor causes larger atmospheric features and variations.

The process was repeated with the surface temperature as well, and this can be seen in Figure 4.3. The bins chosen were created in the same way as the CWV values. There is not an obvious relationship between the LST error and the ground temperature, although the error generally increases between 250 and 330 K.

4.2 Split Window Sensitivity Results

To determine the sensitivity of the split window equation, the radiance and brightness temperature are biased, according to Equation 3.1, to see the resulting effect on the LST as described in Section 3.3.1, and the results are shown in Figure 4.4. There are a few important observations to be made from this plot, the first being the difference between biasing the radiance of the individual bands. For Band 10, the error in the LST has a direct correlation to the change in radiance, while Band 11 has an inverse correlation to the change in radiance. This may not make sense at first, as one would expect
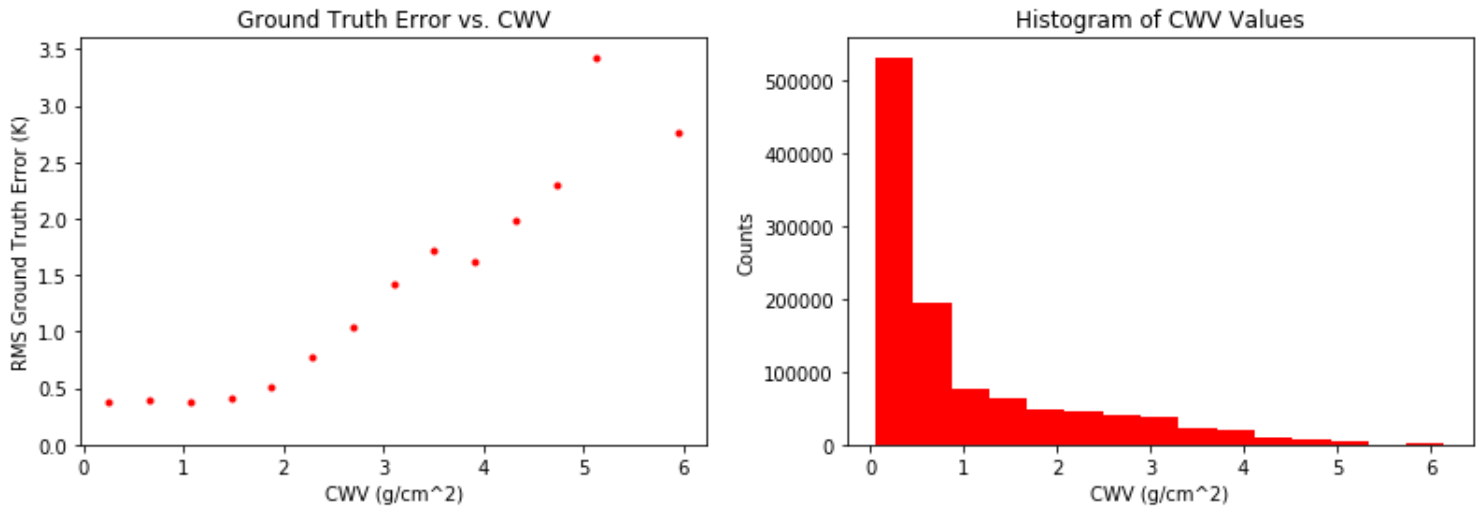
Figure 4.2: (a) Showing ground truth error as a function of CWV. I used 40 bins to split up the CWV values. (b) Shows the histogram of CWV values in the 15 bins used.
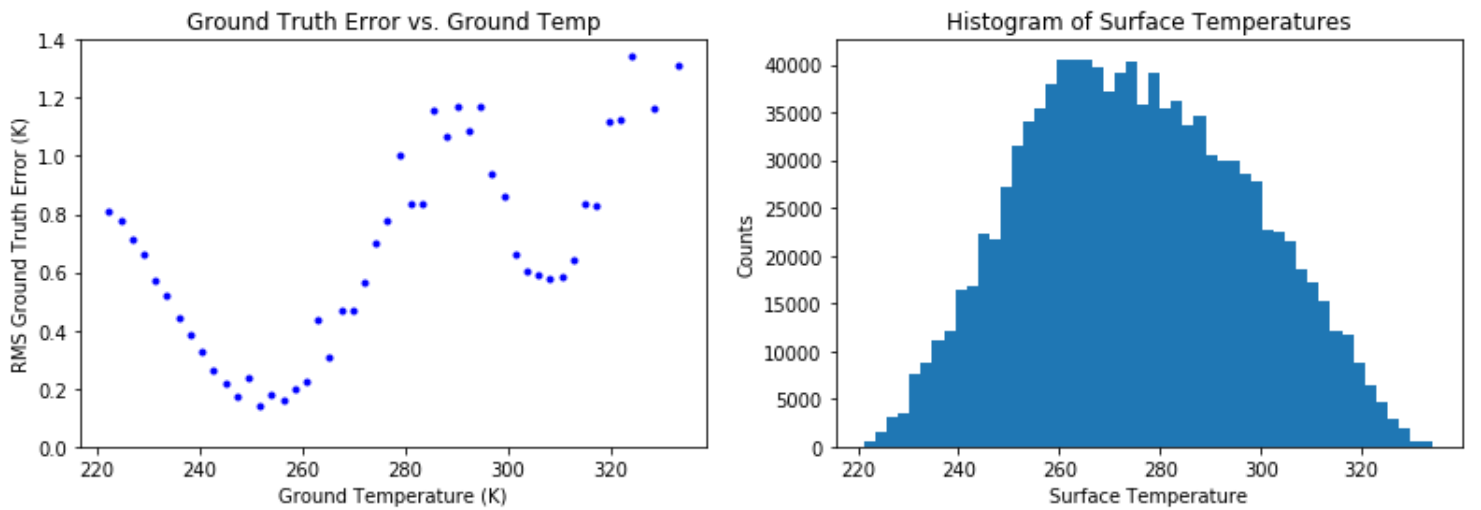
Figure 4.3: (a) Showing ground truth error as a function of CWV. I used 15 bins to split up the CWV values. (b) Shows the histogram of CWV values in the 15 bins used.
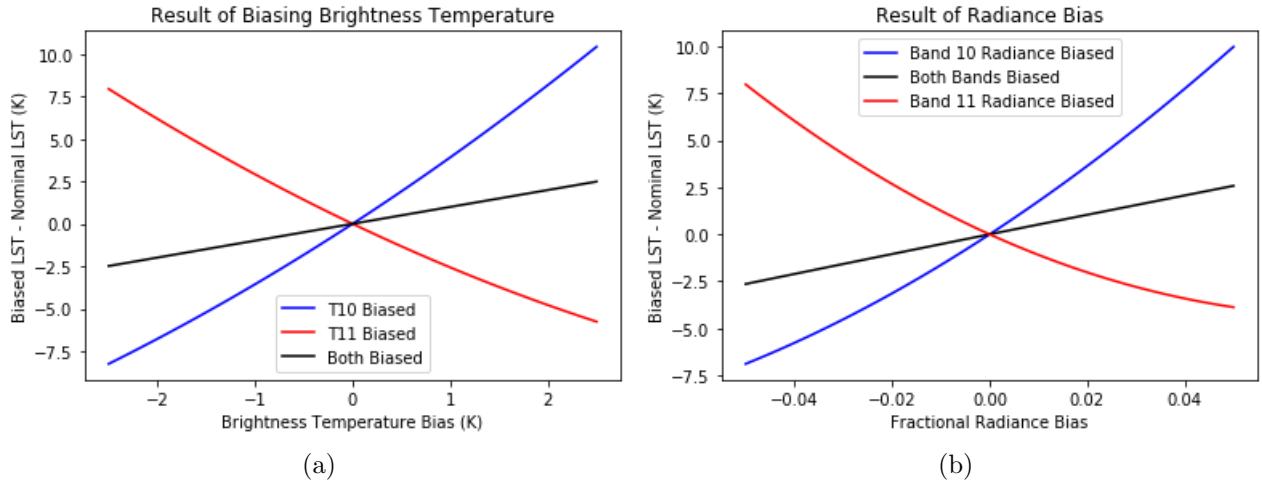
Figure 4.4: (a) shows the result of biasing the Brightness temperature of the two bands by $+/- 2.5\ K$. (b) shows the result of biasing the radiance by $+/- 5\%$. For both of these plots, the MLW atmosphere was used, and the surface temperature was set to 270.

the LST to increase as the brightness temperature increases, even if it is just a single temperature.

The explanation for this comes from the Split Window Algorithm itself (Equation 2.4) and the coefficients shown in Table 4.1. The two main terms are the sum and difference of the two brightness temperatures, with corresponding coefficients b_1, b_2, and b_3 for the summation terms, and b_4, b_5, and b_6 for the difference terms, where b_1 and b_4 have the largest impact. Ignoring the emissivity terms, any change to T_{11} will result in a change to the LST of $\delta T_{11}(b_1 - b_4)$. Looking at Table **??**, b_4 is larger than b_1 in all of cases, which will explain why the LST will decrease as T_{11} increases.

Since we know how altering a single band effects the LST, we also want to see how altering both of them by different amounts in combination effects the LST. These results are shown in Figure 4.5. This shows the results for three different surface temperatures in order to compare a range of scenarios. There are a few interesting observations to make, the first being that the LST increases as the Band 10 radiance increases, and decreases as the Band 11 radiance increases, as expected. For these three different temperatures, it is clear that higher surface temperatures are more sensitive to increases in signal. Also, there is a region where the LST is unaffected. There is an approximately linear curve where the difference between the nominal LST and the LST with biased radiance values are the same, shown as a red curve. It is interesting to note that the curves are not the same for each surface temperature. The main takeaway from these figures is that extra signal in each of the bands has unique effects that can change with the surface temperature.

4.3 Split Window Summary

This chapter has shown the results of several preliminary studies relating to the Split Window Algorithm. The coefficients for the Split Window Algorithm were estimated for multiple conditions This includes the condition where atmospheres with relative humidity above 90% are ignored, which will be the coefficients used throughout this study.

The accuracy of the Split Window Algorithm using these coefficients

(a) 250 K	(b) 290 K	(c) 330 K
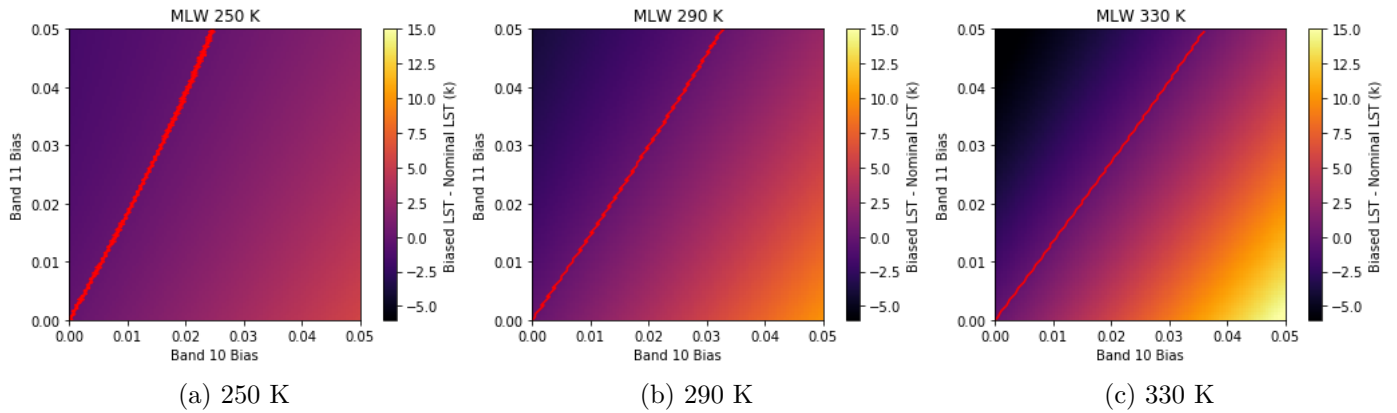
Figure 4.5: This figure shows the result of increasing the radiance in bands 10 and 11 by a certain fraction. The red line down the middle is where the error is zero. Each image contains a different surface temperature, but the scale for the color bar is held the same in order to showcase the difference between them.

were explored in detail, showing that it performs well for most scenarios, with 93.6% of the predicted LST values were within +/- 1 K of the actual surface temperature. The CWV of the atmosphere was shown to have a significant effect on the LST accuracy, and the surface temperature does not have seem to have a noticeable effect on it.

The sensitivity study showed that the two bands respond very differently to an increase in signal. When the Band 10 signal increases, the predicted LST increases. However, when the signal in Band 11 increases the predicted LST decreases. Signal added to each of the bands in different amounts has a combined effect, and the difference in LST could be zero in some special cases, even with significant amount of added signal to each band. It was also

39

shown that this effect is strongly dependent on the surface temperature. These results will be significant for the stray light study.

Chapter 5

Band Study Results

This Chapter will discuss the results of the Band Study, where the methods are described in Section 3.4. The sections of this chapter will show how sensitive the LST derived using the Split Window Algorithm will be to alterations in the bands of TIRS-1, in order to inform requirements for future thermal Landsat instruments. The alterations to the bands include shifting, widening and changing the shape of the RSR's of TIRS-1.

5.1 Methodology Check

In order to make sure the procedure that is used in this study works as expected, the shifting and widening of the bands will be performed on simple spectral radiance curves to make sure the results are as expected. This is done with a completely flat spectra, which is shown in Figure 5.1. This curve has a constant value of 7.5 $W/m^2/sr/micron$. The results of sampling this with shifted bands are shown in Figure 5.2. The results of sampling this with widened bands are shown in Figure 5.3. These figures show that the band averaged radiance does not change, as expected with a flat spectra.

41
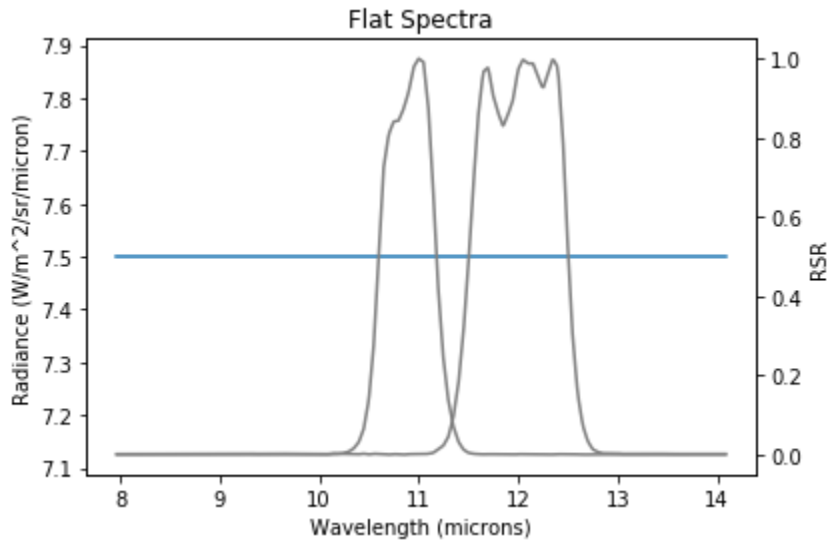
Figure 5.1: Flat spectra used to check methodology.

(a)

(b)
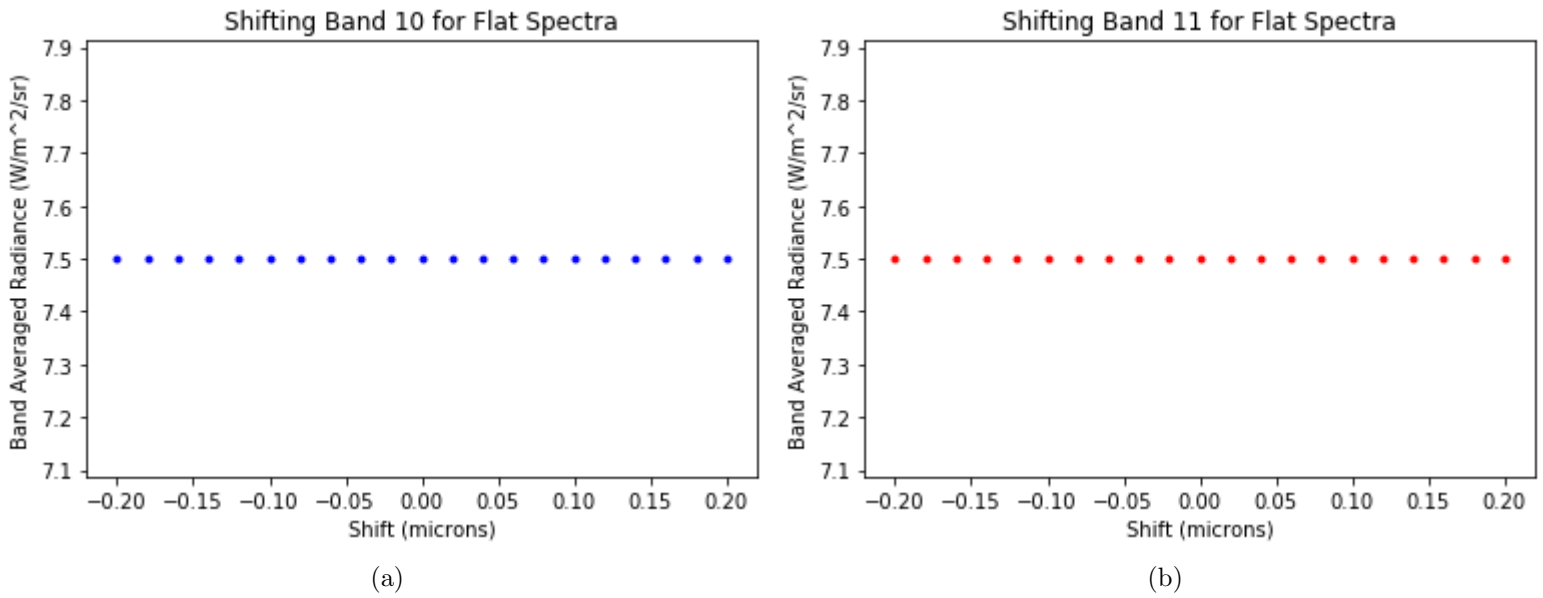
Figure 5.2: Sampling flat spectra with shifted bands.
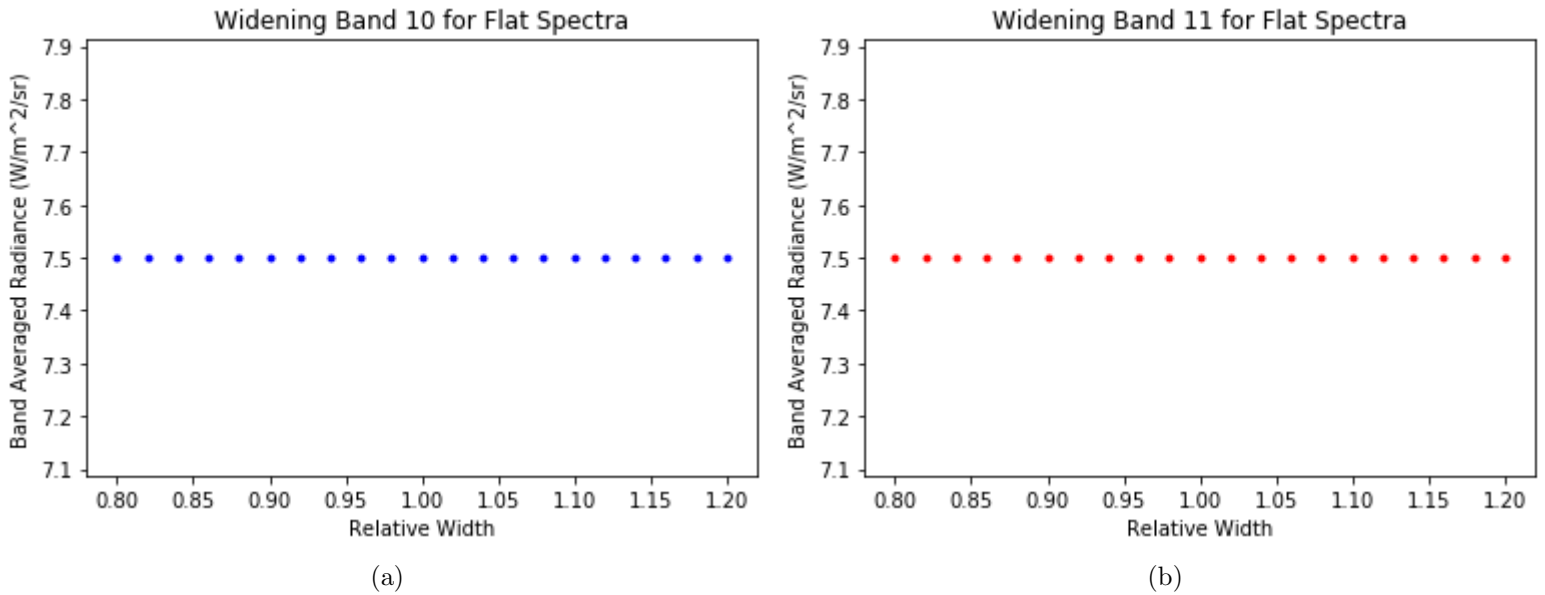
Figure 5.3: Sampling flat spectra with shifted bands.

5.2   Shifting of Bands

Recalling Section 3.4.1, the LST estimated using measurements will be compared to the LST measured with the nominal bands. The difference between them will be used to determine if this will have a significant impact. In both cases, the LST will be estimated using the Split Window coefficients from the nominal bands.

Figure 5.4 shows the result of shifting the bands by +/- 0.05 μm, with a spacing of 0.005 μm between points. Small shifts of the bands can result in significant errors in the retrieved LST.

It is clear from figure 5.4 that shifting Band 11 causes significantly

43
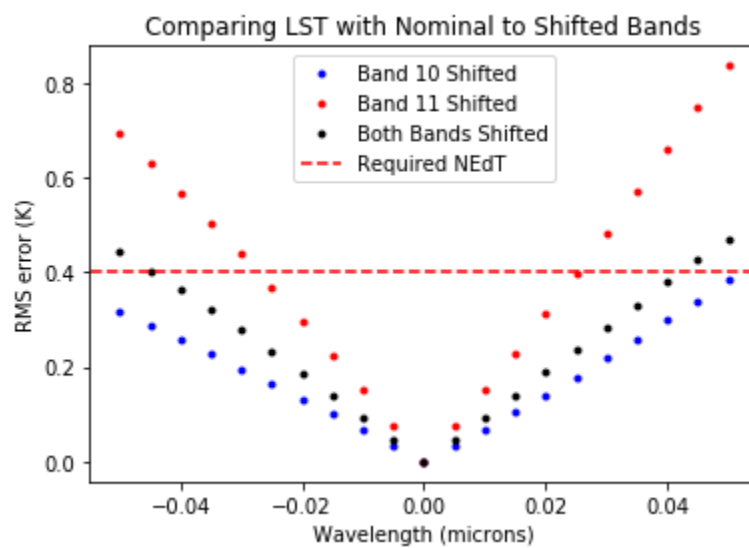
Figure 5.4: This figure shows the result of shifting the bands by a small amount. I show the results of shifting the each band separately, as well as both of the bands by the same amount. The required NEdT value is shown as a reference.

higher error than Band 10. This is most likely the result of the location of the bands on the spectra, relative to absorption features, such as seen in Figure 3.1.

As seen on the plot, a shift of approximately $+/- 0.03$ μm in each band results in an error that is greater than the NEdT. Similarly a shift of approximately $+/- 0.02$ μm in just Band 11 and $+0.04/-0.05$ μm in just Band 10 results in the same error.

5.3   Widening/Narrowing of Bands

Similarly to the shifting of the bands, the width of the bands is also an important parameter to consider. Using the procedures described in Section 3.4.1, the bands were widened/narrowed by a factor of 0.8 to 1.2 of the original width. These values were intentionally chosen in order to produce an error that exceeds the NEdT.

Figure 5.5 shows the results of widening/narrowing the bands, and there are some obvious similarities between the shifting and width of the bands. Once again there is a significant difference between individually altering bands 10 and 11, but in this case Band 10 is lower by over a factor of 5, instead of a factor of 2 as seen in the shifting study. It is also obvious that when altering both bands, the error is almost the same as just altering Band 11. This is most likely due to how much smaller the error in Band 10 is compared to Band 11, so when they are combined, the difference is negligible.
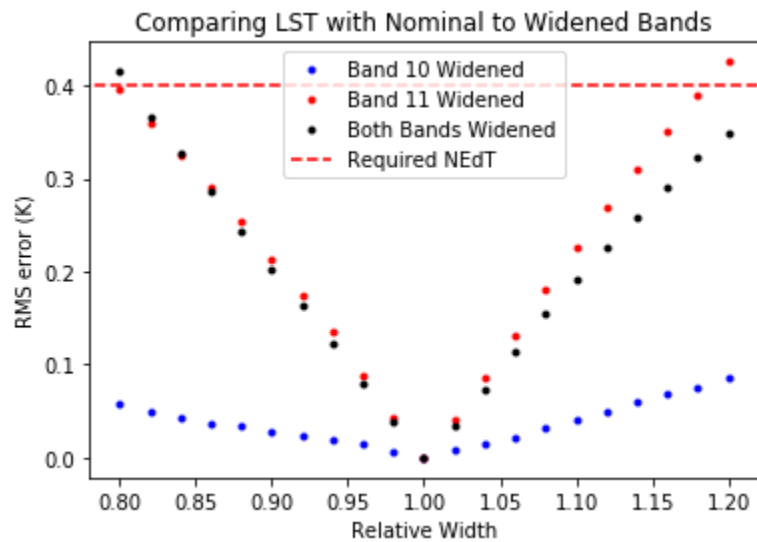
Figure 5.5: This figure shows the result of widening the bands. The relative width values used are between 0.8 and 1.2, with a spacing of 0.02 between points. The required NEdT value is shown as a dotted red-line as a reference for the error. These ranges of relative width were used in order to create an error greater than the required NEdT.
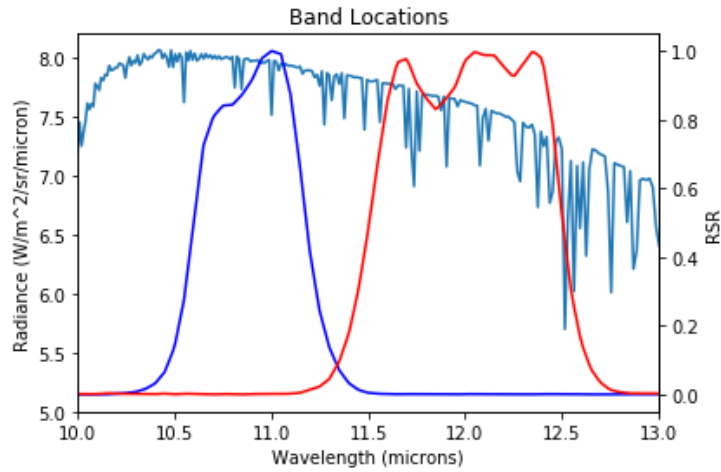
Figure 5.6

5.4 Further Analysis of LST Error

The previous results only show the RMS LST error for over a million different simulated measurements, without looking into any outliers or any contributions due to other factors. This section will look at the distribution of LST errors, and their dependence on factors such as atmosphere and emissivity.

The placement of the bands relative to the absorption features seems to be the best explanation as to why the bands respond so much differently. Figure 5.6 shows the bands relative to a spectral radiance curve, and it is clear that Band 11 is located near many more absorption features, including a large feature around 12.5 μm.
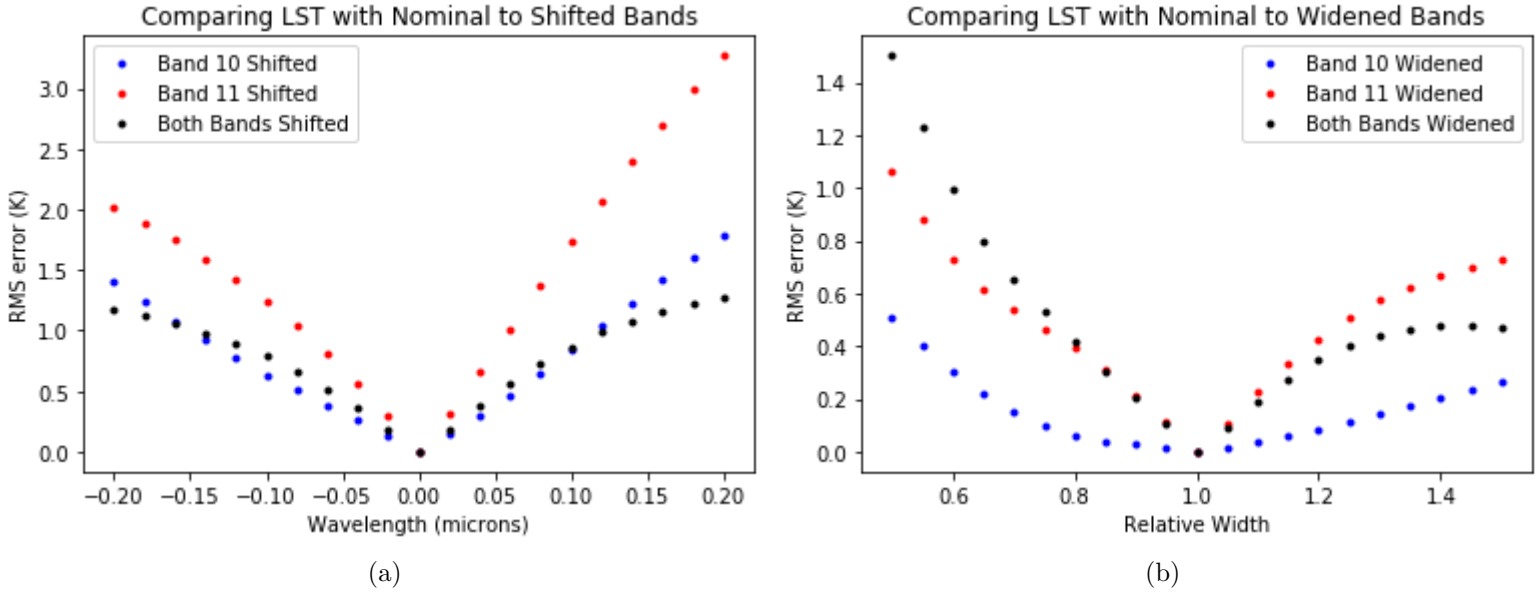
Figure 5.7: Results for extending the shifting and width values from the previous studies

5.4.1 Extending Shifting and Widening Values

The previous values for shifting and widening of the bands were chosen based off of creating RMS errors of at least 0.5 K, but this can also be extended to larger values. Figure 5.7 (a) shows the result for increasing the shift values to +/- 0.2 μm, and Figure 5.7 (b) shows the results for changing the width by +/- 50%.

For both of these cases, the plots become more non-linear and less symmetric with respect to the nominal bands. This is most noticeable with the width of the bands, as decreasing the width seems to have a much greater
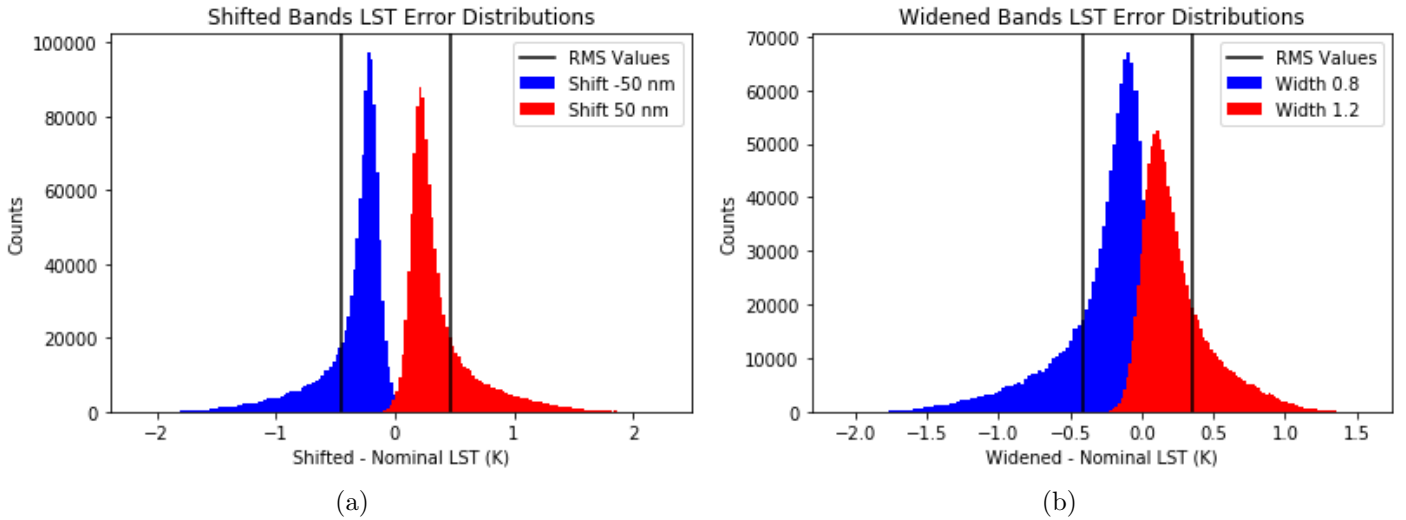
Figure 5.8: This figure shows the histogram of LST difference between the shifted/widened bands and the nominal bands. (a) shows the results for shifting the bands, for a shift of +/- 50 nm. (b) shows the results for widening the bands, for a relative width of 0.8 and 1.2. The black lines show the position of the RMS values relative to the distribution, which were made negative for the distributions with predominately negative values.

effect than increasing the width.

5.4.2 LST Error Distributions

This first section will investigate the distribution of the LST difference between the shifted/widened bands and the nominal bands. As a reference, the max values from the previous shifting (+/- 50 nm) and widening (relative width of 0.8 and 1.2) study will be used to compare to the nominal bands. Figure 5.8 shows the histogram of all errors for these scenarios.

These distributions show that there are many cases where the estimated LST will be over 1 K from the nominal estimated LST, and a few by as much as 2 K. These errors are significant, as researchers desire a LST product accurate to within 1 K.

5.4.3 Atmospheric Contributions

As stated in Section 3.1, the TIGR atmospheres are split into five different categories: Tropical, Mid-Latitude 1, Mid-Latitude 2, Polar 1 and Polar 2. As a reminder, when atmospheres with a relative humidity greater than 90% are removed, this leaves us with: 369 Tropical, 224 Mid-Latitude 1, 216 Mid-Latitude 2, 95 Polar 1 and 485 Polar 2 atmospheres.

To see if there is any correlation between the atmosphere type and the LST error due to shifting or widening of the bands, the RMS LST error was calculated for all of the scenarios for each atmosphere (7 temp values and 113 emissivities), then these residual errors were categorized into the five atmosphere types. This was performed for shifting both of the bands by +/- 50 nm, as well as altering the width by a factor of 0.8 and 1.2 for each of the bands. These values were chosen since they are the extreme values used in the above sections.

Figure 5.9 shows the histogram of RMS LST errors for the five different atmosphere types. The first interesting result is that the tropical atmospheres have higher LST errors than any of the other atmosphere types, and this is

(a)

(b)

(c)

(d)

Figure 5.9

51
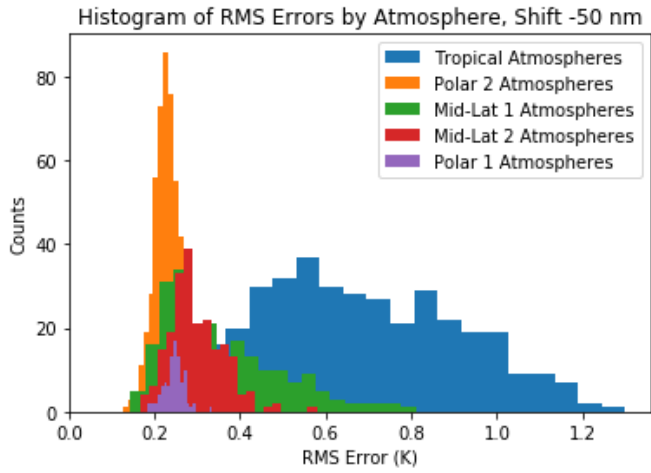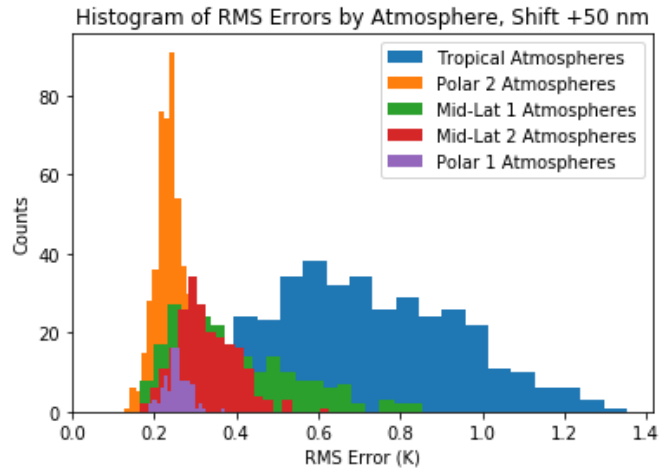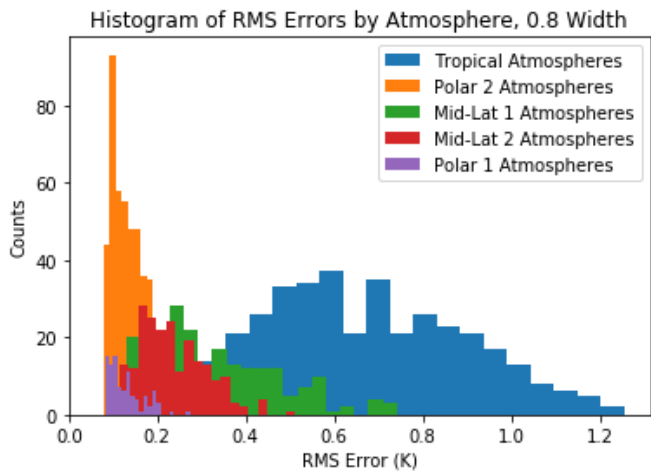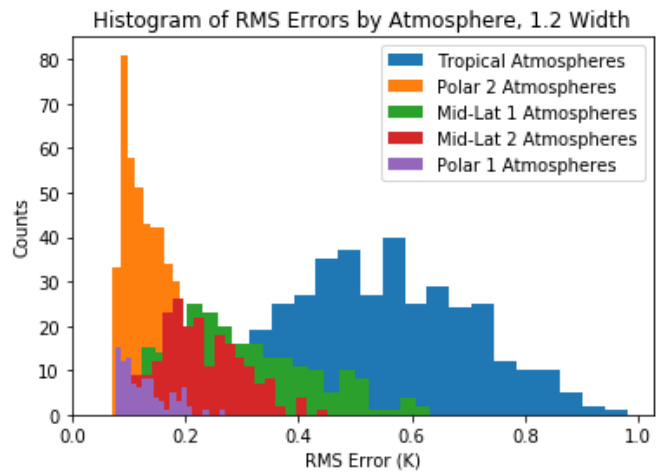
consistent between all four of these figures. It is also noticeable that the Polar 1 and Polar 2 atmospheres have similar distributions to each other, as well as the Mid-Lat 1 and Mid-Lat 2 to each other. It is also important to note that all four of these figures are consistent to each other, and the atmospheres react consistently to shifting left/right and widening/narrowing. In other words, each atmosphere will respond similarly to shifting the bands to the left and right, as well as widening and narrowing of the bands.

5.4.4 Emissivity Contribution

In addition to the atmosphere type, uncertainty in emissivity will likely have an effect on the LST error. The 113 emissivities are split into three categories: 74 soil/minerals, 26 vegetation, and 13 water/ice. In the same way as the atmospheres, the RMS LST error is calculated for these three categories for the min/max of the width and shift values used above.

Figure 5.10 shows the histogram of RMS LST error for these three emissivity categories. There is not a distinct difference between these three categories, and it appears that they are centered around the same mean value. This may be due to the lack of samples, as there are only 24 vegetation and 13 water/ice emissivities, but there is no evidence to suggest that there is any real correlation between the type of material and the LST error due to shift or width.

In addition to the type of emissivity, there might also be a relationship
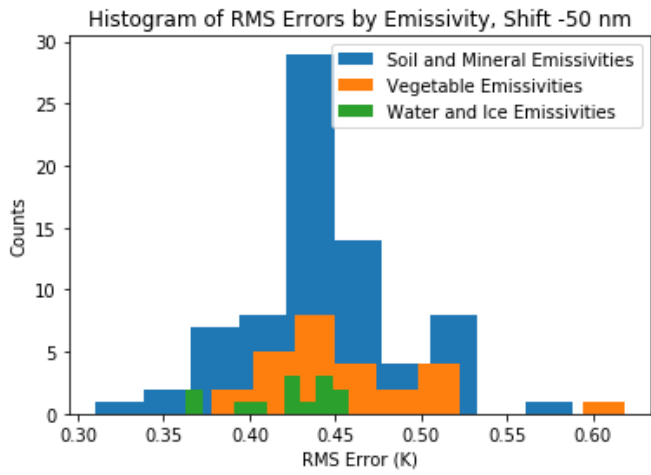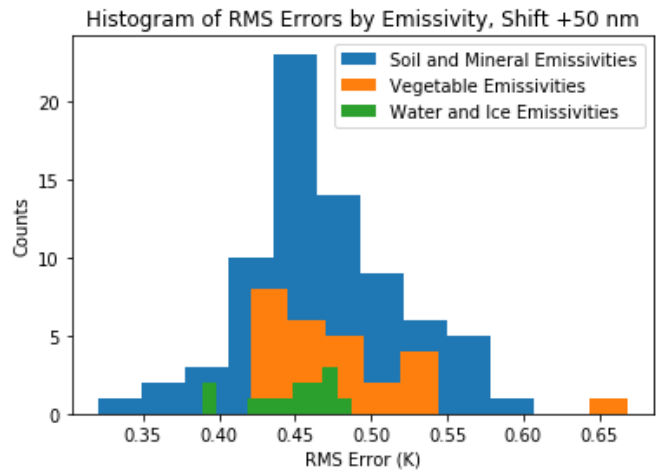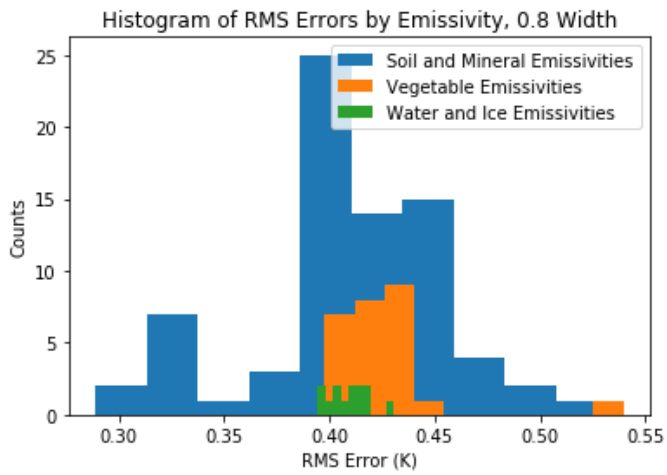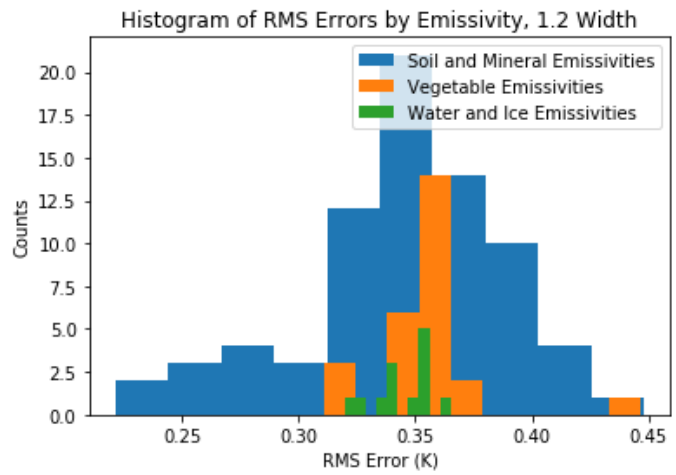
Figure 5.10: Histograms of LST errors split into emissivity categories.
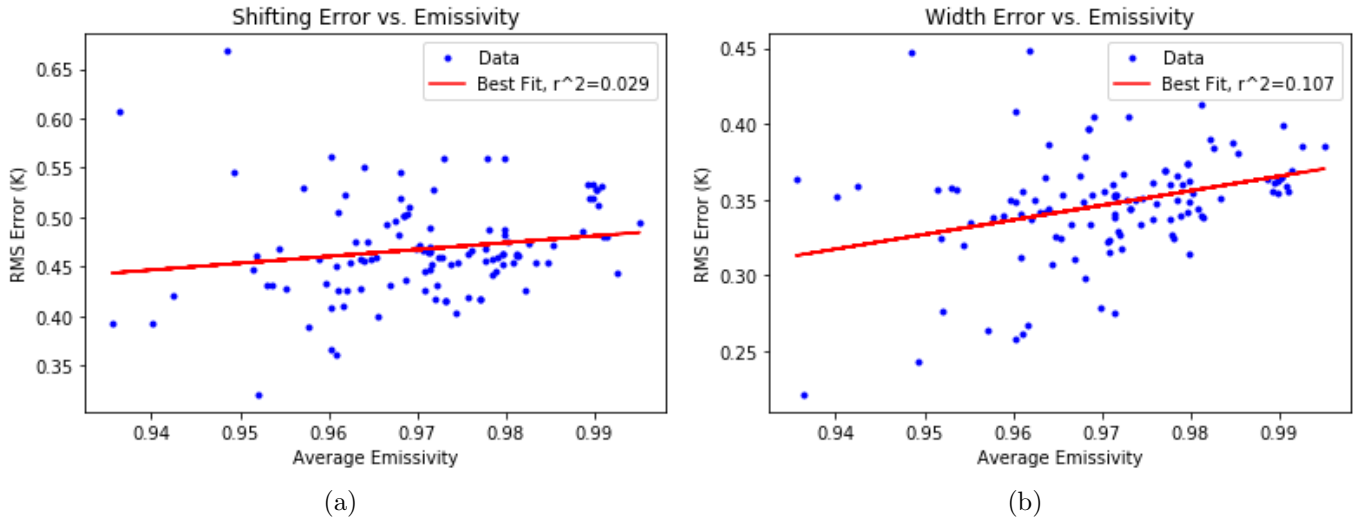
Figure 5.11: This figure shows the relationship between LST error and emissivity. (a) shows the results for shifting the bands. (b) shows the results for widening the bands.

between the average emissivity between the two bands and the LST error. To assess this relationship, a linear fit between the RMS error vs average emissivity for shifting and widening of the bands was investigated, and found there is little to no correlation between the two. Figure 5.11 shows these results. For the shifting error, $r^2 = 0.029$, and for the width error, $r^2 = 0.107$. These very low correlation values imply that there is in fact no relationship between emissivity and LST error with respect to the band-alteration studies presented here.
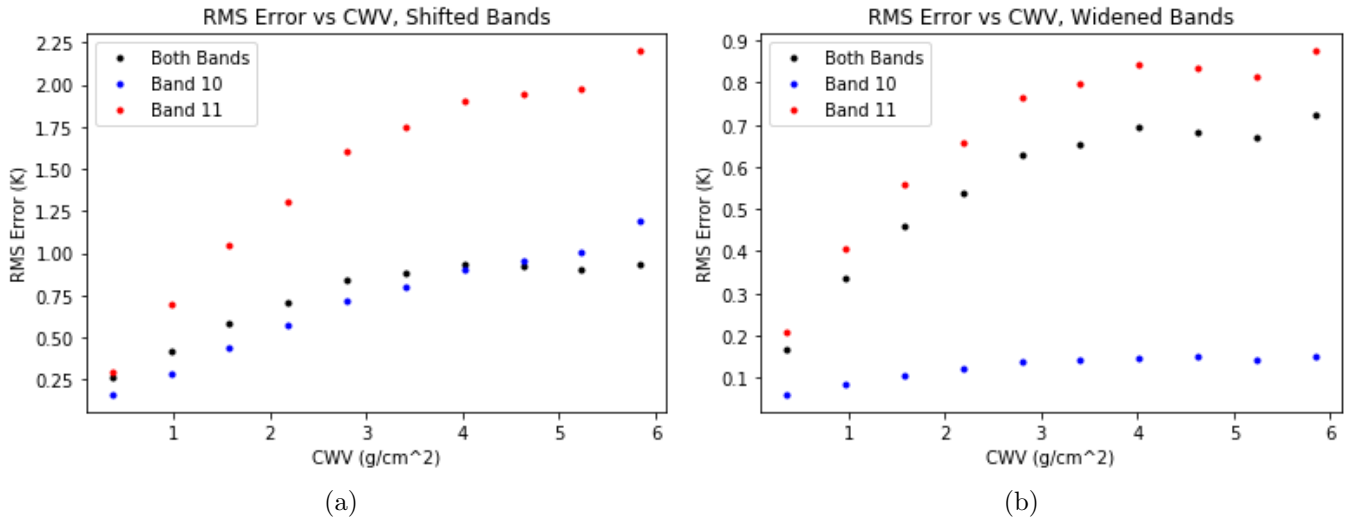
Figure 5.12: This figure shows the relationship between LST error and CWV. (a) shows the results for shifting the bands. (b) shows the results for widening the bands.

5.4.5 CWV Contribution

The next part of this study will investigate the relationship between the LST error and CWV. To do this, the predicted LST values are split into bins based off of the CWV of the atmosphere. The CWV values are split into 10 equally spaced bins, between 0 and 6 g/cm^2, and the RMS difference between the LST predicted with the nominal and shifted/widened bands for each of these CWV bins are calculated.

These results are shown in Figure 5.12. There is a clear relationship between the CWV and the resulting error. This is intuitive, as the more water vapor in the atmosphere, the larger the absorption features will be. As a result,

if the bands are shifted or widened, they will sample more of these features, which will have a significant effect on the band-averaged radiance.

5.5   Band Shape Results

While the previous section looked at the results of altering the nominal bands, this section will look at how much the shape of the bands can affect the LST. The first part of this will examine why Band 11 seems to be much more sensitive to shifting or widening than Band 10. There are two possibilities: the shape of Band 11 or the position of Band 11 is responsible for this sensitivity. By replacing the shape of Band 11 with that of Band 10, we can determine which of these are more important.

Looking at the shifting results shown in Figure 5.13, it is clear that the shape is a significant factor for the shifting of the bands. The LST error in Figure 5.13(a) is significantly smaller than in Figure 5.4 and Figure 5.13(b), by about a factor of two in all cases. It is especially interesting to note that when the Band 11 RSR is replaced with the Band 10 RSR, there is very little difference between shifting Band 10 or Band 11. However, when the Band 10 RSR is replaced with the Band 11 RSR, there is in fact a significant difference between the two.

In case (a), it is clear that when both bands are shifted, the LST error due to shifting is significantly less than with the nominal bands, but for case (b) it is nearly the same as the nominal bands. The final conclusions from

56
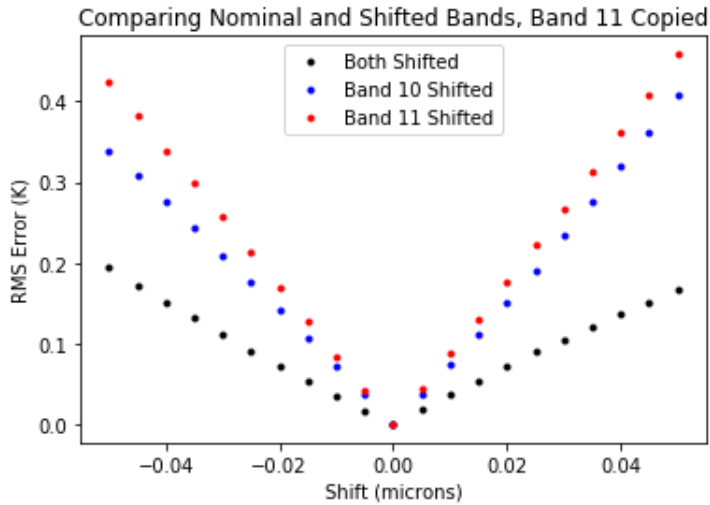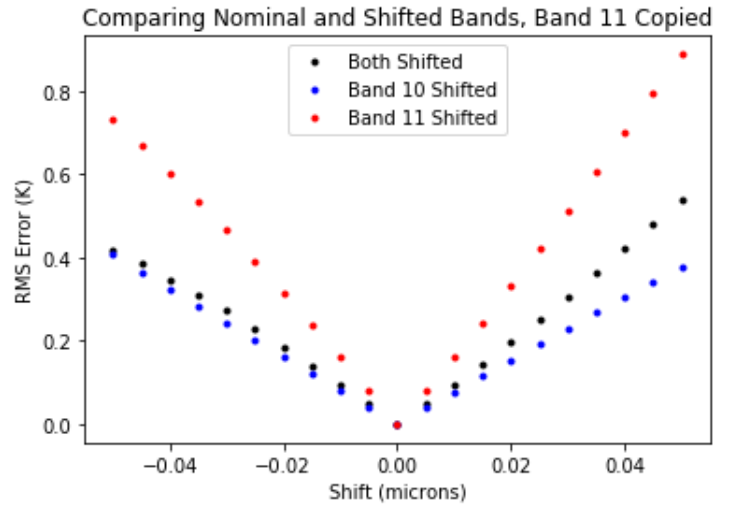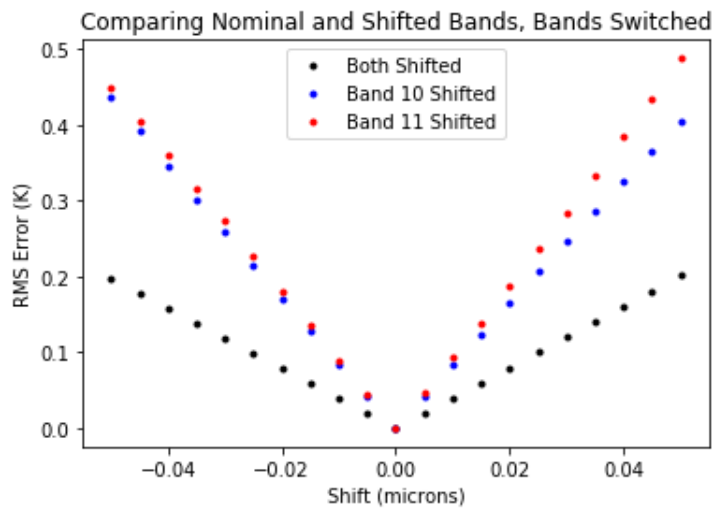
Figure 5.13: This figure shows the results when replacing the shape of one band with the other band and then shifting the bands. (a) shows the results for replacing Band 11 with the shape of Band 10. (b) shows the results for replacing Band 10 with the shape of Band 11. (c) shows the results for switching the shapes of Band 10 and 11.

these results are that the shape of the bands clearly have a significant effect when it comes to the shifting error, and that the shape and location of Band 11 seem to be the main factor.

The results for the width is shown in Figure 5.14. These results are not as significant as for the shifting of the bands, as the LST error is about the same for all of these scenarios. The biggest exceptions are when only shifting Band 10. When using the nominal band, the width barely has any effect, at least when compared to the other examples, but when replaced with the Band 11 shape the error more than doubles. It is also apparent that the largest LST error occurs when the Band 11 RSR is copied, and only Band 11 is widened. It is interesting to note that the nominal case shown in Figure 5.5 has higher LST error when both of the bands are widened than any of the scenarios shown in Figure 5.14. The main takeaways from this study is that the Band 11 shape is more sensitive to widening, and the location of Band 11 is also more sensitive to widening.

Figure 5.15 shows the results of shifting and widening of the Gaussian and rectangular bands. These figures are the equivalent of Figures 5.4 and 5.5 which use the nominal bands.

The results for shifting and widening of the Gaussian bands are shown in Figures 5.15 (a) and (b), respectively. Comparing this to the nominal bands, one difference is the magnitude of the LST errors. The shifting and widening of the Gaussian bands both have a smaller effect on the retrieved LST, the

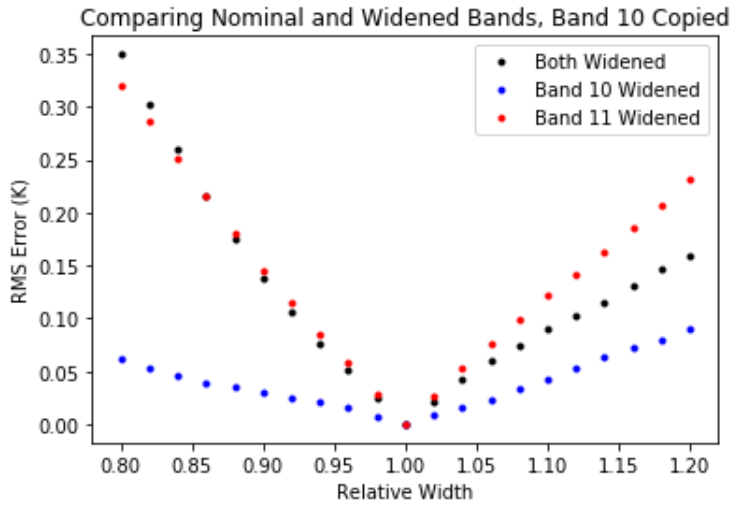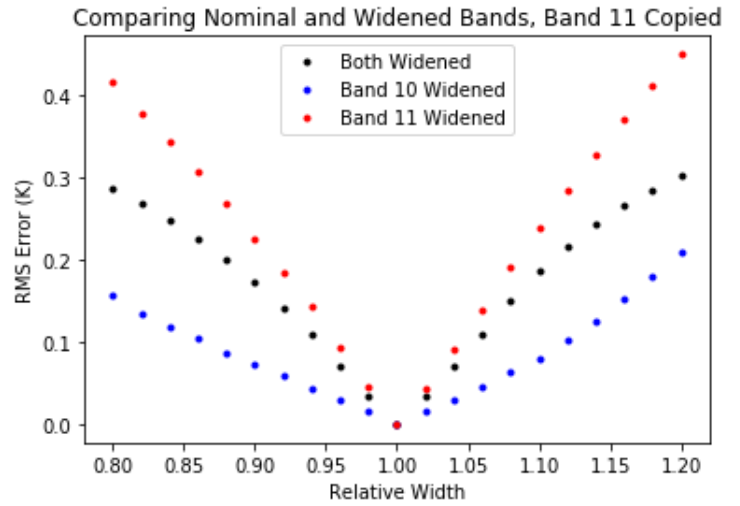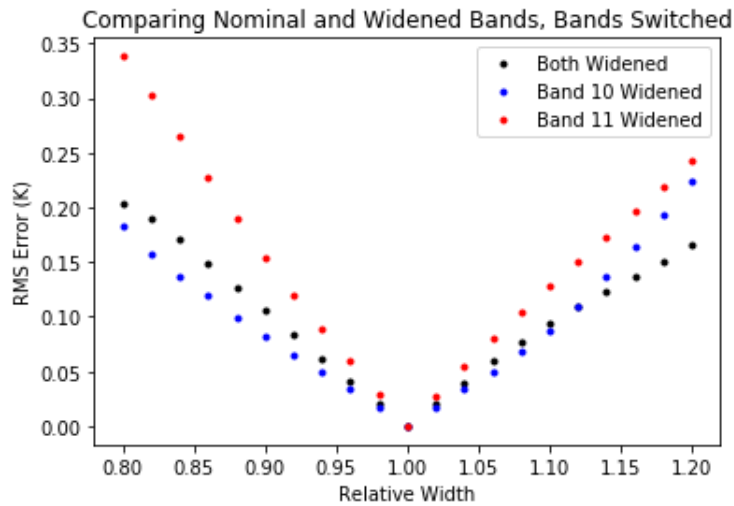Figure 5.14: This figure shows the results when replacing the shape of one band with the other band and then shifting the bands. (a) shows the results for replacing Band 11 with the shape of Band 10. (b) shows the results for replacing Band 10 with the shape of Band 11.
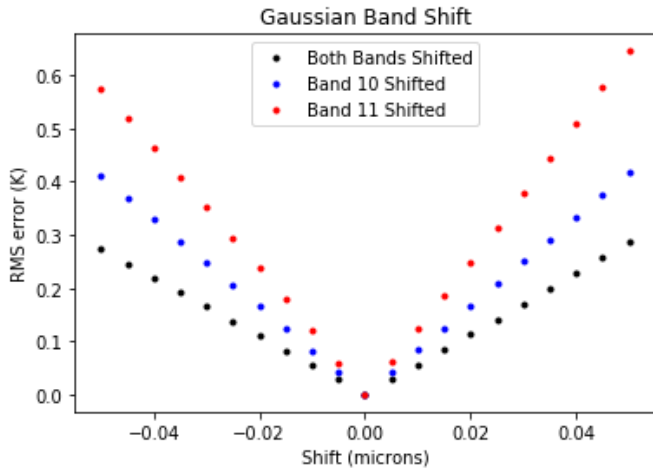
(a) Gaussian Width
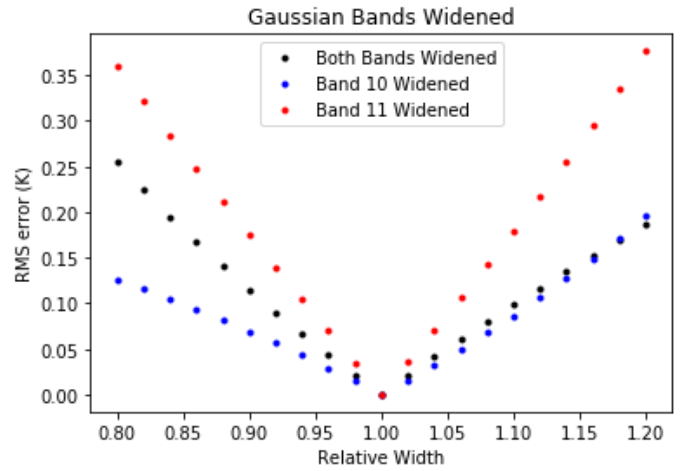
(b) Gaussian Shift
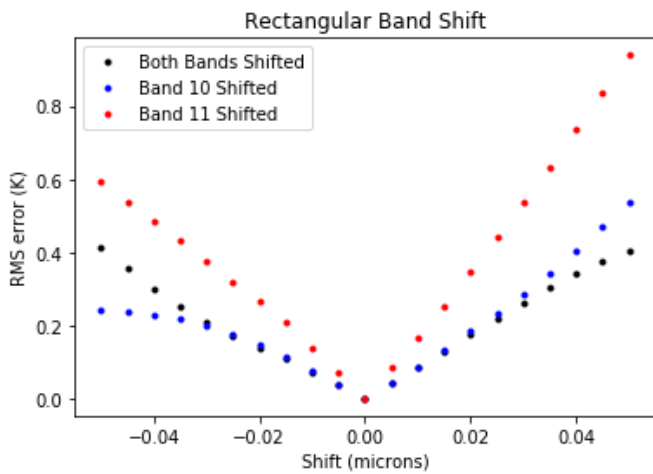
(c) Rectangular Width
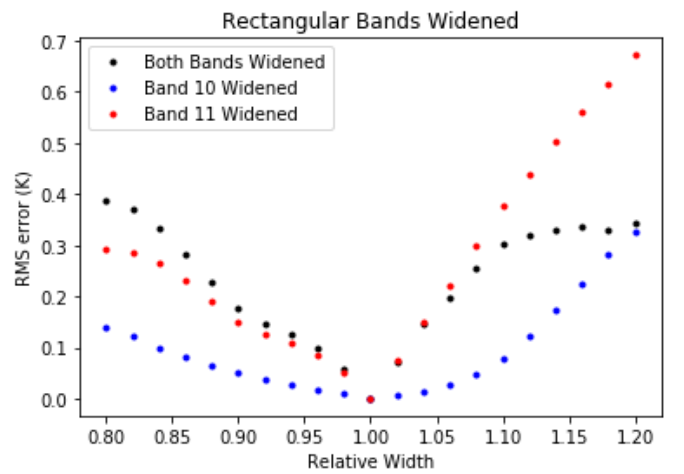
(d) Rectangular Shift

Figure 5.15: This figure shows the results of shifting and widening the rectangular and Gaussian bands. (a) shows the results of shifting the Gaussian bands. (b) shows the results of widening the Gaussian bands. (c) shows the results of shifting the rectangular bands. (d) shows the results of widening the rectangular bands.

only exception being when only Band 10 is widened.

The results for shifting and widening of the rectangular bands are shown in Figures 5.15 (c) and (d). In this case, the LST error seems even larger than the nominal bands for most cases, and is asymmetric to whether the bands are shifted to the right or left, or widened or narrowed.

The next results are looking at combining the nominal and Gaussian/rectangular bands. The results are shown in Figure 5.16. The RMS error shown here is the RMS difference between the LST predicted with the nominal bands and the LST predicted using the altered bands. These results show that there is not a significant difference between these different bands, even when they are completely replaced with the Gaussian or rectangular bands.

5.6   Band Study Summary

The results from these studies show that uncertainty in band shape can have a significant effect on the retrieved LST, and some properties are more significant than others. The results from the band shifting seem to be the most significant, with shifts of less than 0.05 μm causing an RMS difference between the nominal and shifted LST exceeding the $NEdT$. This shows that any small shifts in the bands may actually have noticeable effects on the Split Window LST product. Looking at the width of the bands, they would need to be widened or narrowed by a significant amount, at least $+/- 15\%$.

When diving deeper into the effect that the bands can have on the LST,
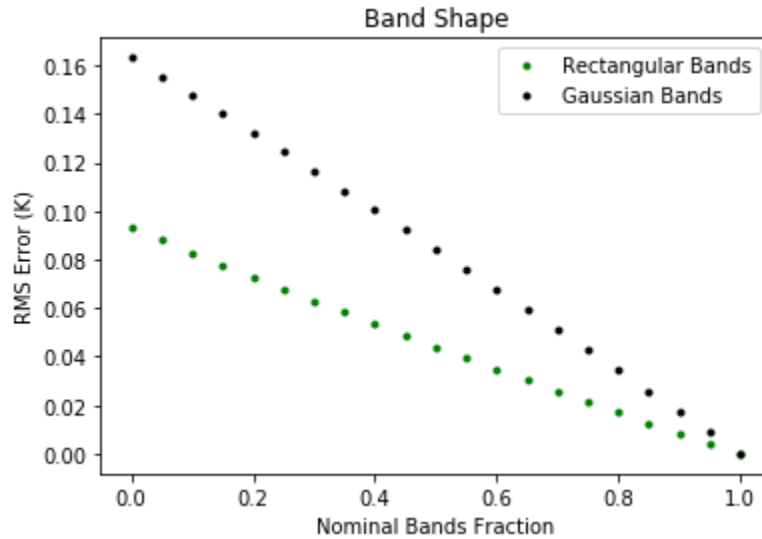
Figure 5.16: This figure shows the results for combining the nominal and Gaussian/rectangular bands.

it can be seen that the distribution of LST errors can be as high as +/- 2 K for a shift of +/- 50 nm. There is also a clear relationship between these errors and the CWV in the atmosphere. The type of atmosphere also seems to have a significant impact on the error, as the error will be significantly higher for tropical atmospheres than the other, less humid atmospheres. There appears to be no correlation between the emissivity and the error.

The band shape study shows that the Band 11 shape has a significant effect when it comes to shifting of the bands, and a small effect on the width of the bands. When combining the nominal bands with rectangular and Gaussian bands, there is not a significant difference between the retrieved LST.

Chapter 6

Stray Light Study Results

This chapter will include the results for determining the impact of stray light on retrieved LST. The details and the methods used for these studies are described in Section 3.5. These studies are performed in order to characterize the possible impact that stray light may have on retrieved LST, using TIRS-1 and TIRS-2 as references.

The first section in this chapter, Section 6.1, includes the preliminary results, which only consider blackbodies in order to get a baseline of the impact of stray light. Section 6.2 will explore how the results change when emissivity is included. Section 6.3 will explore how the results change with different atmospheres. Section 6.4 compares the difference between different magnitudes of stray light, such as those observed with TIRS-1 and TIRS-2 instruments. Section 6.5 compares stray light magnitudes on TIRS-2 for the different detectors, specifically the peak of the 13 and 22 degree stray light, which have peaks of 0.20 % in Band 10 and 0.20 % in Band 11, and 0.24 % in Band 10 and 0.32 % in Band 11, respectively [23].

Section 6.6 compares the error in the LST due to stray light to the residual error due to the Split Window Algorithm. Section 6.7 looks at the

impact that stray light will have on LST estimated with the Single Channel Method, and compares it to the Split Window Algorithm.

6.1 Preliminary Results

This study will look at the impact of stray light on retrieved LST using the Split Window Algorithm. The description of how this study is performed is described in Section 3.5.1, but to summarize involves having a target out of the expected field of view contributing to the signal. Both the in-field and out-of-field targets can have separate properties, such as temperature and emissivity. As a way to get an initial understanding of the impact of the different combinations of in-field and out-of-field sources, blackbody targets were assumed here.

The results from this study are shown in Figure 6.1, where each color represents targets with the same in-field temperature, the x-axis shows the out-of-field temperature, and the y-axis shows the difference between the estimated LST with stray light and the nominal LST. The first observation is that the lower the in-field temperature and the higher the out-of-field temperature, the higher the error. This makes sense, as the out-of-field temperature would make up a much higher percentage of the total signal. For the worst case scenario shown in this plot, where the in-field temperature is 250 K and the out of field temp is 330 K, the out-of-field radiance is 0.78% and 0.93% of the in-field signal for Bands 10 and 11, respectively. This is approximately three times
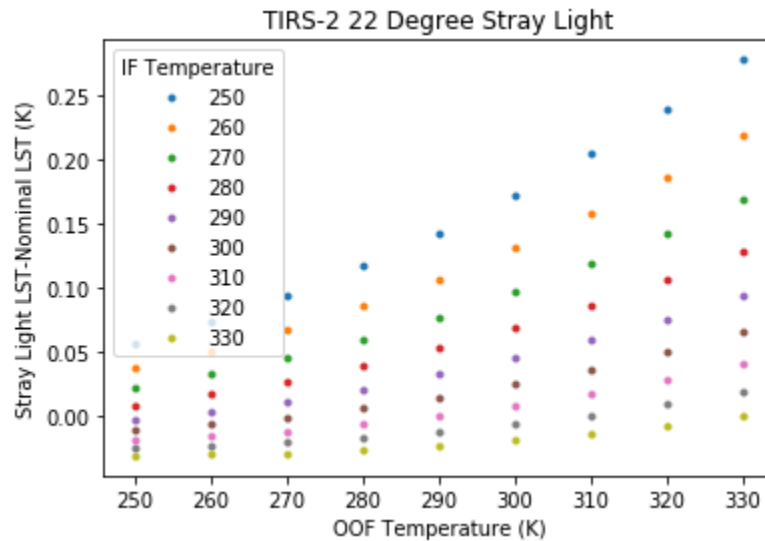
Figure 6.1: These are the preliminary results for the Mid-Latitude Winter atmosphere, with the in field and out of field temperatures ranging from 250 K to 330 K. The error shown is the difference between the LST predicted using the signal with and without stray light.

the stray light if the out-of-field temperature was equal to the in-field. When these temperatures are reversed, i.e. the in-field temperature is 330 K and the out-of-field is 250 K, the percent signal decreases to 0.068% for Band 10 and 0.11% for Band 11, which is about a third of the stray light magnitude.

6.2 Emissivity Contribution

This section will look at the impact that emissivity can have on the retrieved LST when combined with stray light. Now, for every in-field and out-of-field temperature combination we will also have 113*113 different emissivity

combinations. Recall that the previous study only included blackbody targets. This will result in a distribution of errors at each point. The methods used for this section are described in Section 3.5.2. Figure 6.2 shows an example of these distributions, for the MLW atmosphere. These distributions show that there is in fact a wide spread in the errors, which demonstrates that emissivity can introduce significant error in this context. It also shows that as the out-of-field temperature increases, the error distribution retains a similar shape but the mean error increases by a significant amount. This intuitively makes sense, since one would expect the average error to increase as the out-of-field signal increases. It also shows that the higher the in-field temperature, the smaller the effect the stray light will have.

Figure 6.3 shows the results for different temperature combinations, similar to Figure 6.2, but including the emissivity results as well. Each temperature combination now includes the min, mean and max of the distribution due to emissivity. To make the figure less cluttered, only two in-field and four out-of-field temperatures are used. The in-field temperatures are -10 K and +20 K of the lowest layer temperature of the atmosphere (270 K for the MLW atmosphere), and -10 K, 0 K, +10 K and +20 K of the lowest layer temperature for the out-of-field temperatures.

The main takeaway from Figure 6.3 is that different emissivity combinations can result in significantly different results, but the actual magnitude of the error is still relatively small compared to uncertainty in the Slit Window
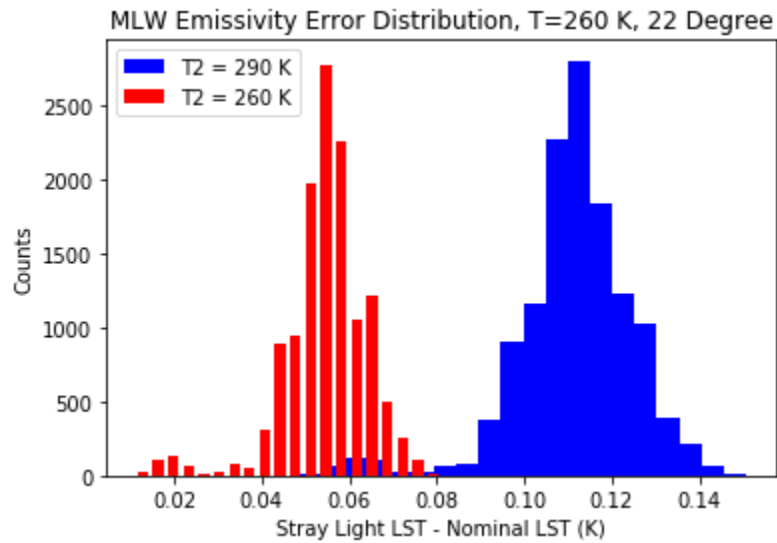
(a)
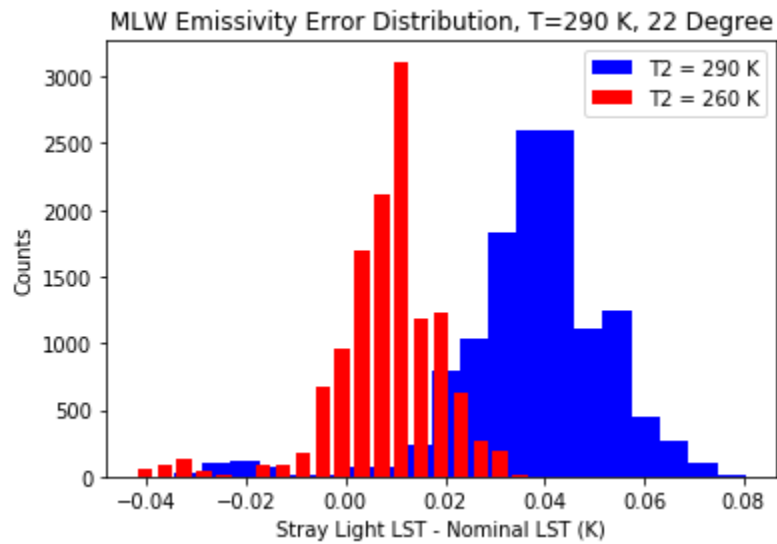
(b)

Figure 6.2: Histogram of errors due to in field and out of field emissivity combinations. The plot in (a) uses the MLW atmosphere with an in field temperature of 260 K, and an out of field temperature of both 260 K and 290 K. The plot in (b) uses the MLW atmosphere with an in field temperature of 260 K, and an out of field temperature of both 260 K and 290 K.

67
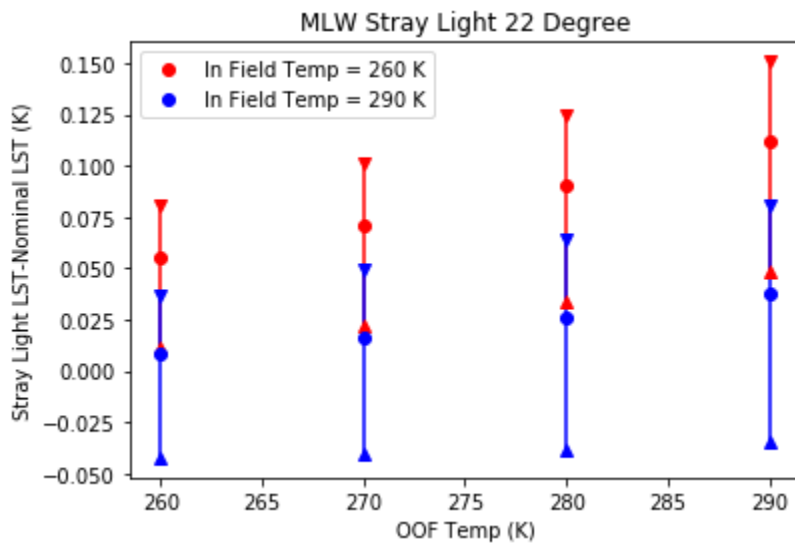
Figure 6.3: This figure shows the ranges of errors at each temperature combination due to emissivity. The red points represent the lower bound (-10 K) of a realistic in field temperature, and the blue points represent the upper bound (+20 K) of a realistic in field temperature. The center dot at each point shows the average difference, and the bars represent the min and max values of each error distribution (such as the ones shown in figure 6.2).

process. The maximum errors will be about 0.150 K, which is still well below the uncertainty in the LST.

6.3 Atmospheric Considerations

This section will compare the stray light results for different atmospheres. The MLW atmosphere was used in previous sections for simplicity, but the different atmospheres might be significantly different. The other atmospheres used in this section are the Mid-Latitude Summer (MLS), Sub-Arctic Winter (SAW), Sub-Arctic Summer (SAS) and Tropical (TRP), these all (including MLW) make up the five standard atmospheres used in MODTRAN. The emissivity Min/Max plots for the five standard atmospheres are shown in Figure 6.4.

These figures clearly shows that the distribution of errors is different for each of the atmospheres, especially for the tropical atmosphere. This is likely due to the water vapor content of the atmosphere.

While the distributions are different, the max values are relatively similar between them, where the highest errors are about 0.10-0.15 K. Most importantly, the maximum errors are still relatively small compared to the NEdT. This supports the previous observation that the LST error due to stray light will mostly be negligible compared to any other sources of LST error, for the magnitudes used here.
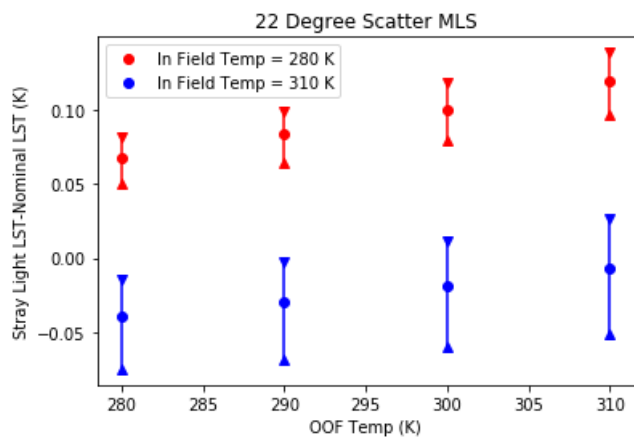
(a) Mid-Lat Summer
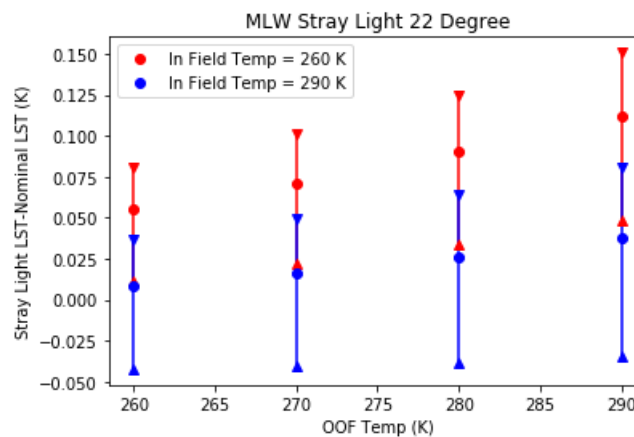
(b) Mid-Lat Winter
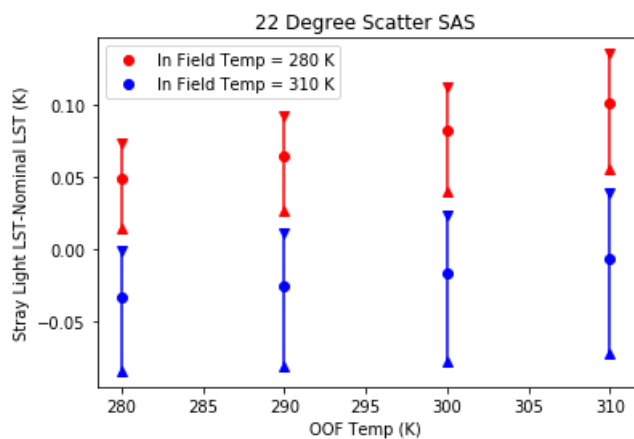
(c) Sub-Arctic Summer
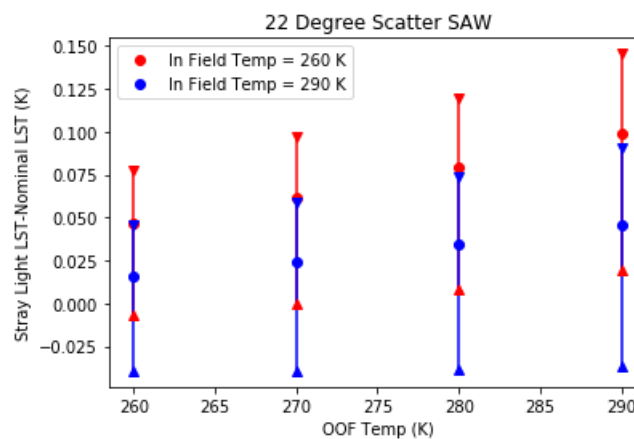
(d) Sub-Arctic Winter
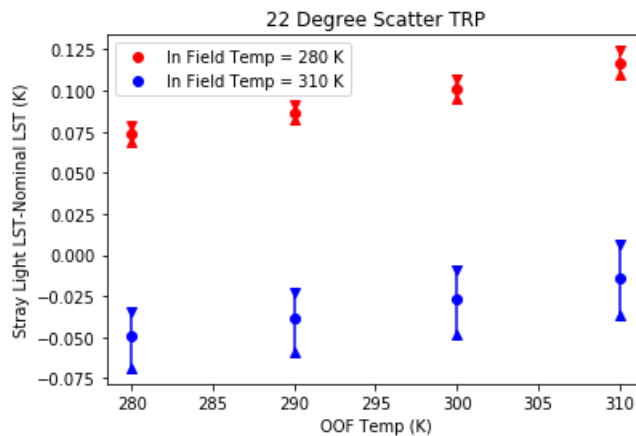
(e) Tropical

Figure 6.4: This figure contains the emissivity distributions for the five standard MODTRAN atmospheres.

6.4 Comparison to TIRS-1 Stray Light

In order to demonstrate how insignificant the stray light error on TIRS-2 is, the same study was repeated using the approximate Stray Light values from TIRS-1. It is reported that in uniform scenes, the stray light magnitude percentage is approximately 2% and 4% in Bands 10 and 11 respectively [4]. It is also observed that in most detectors, the stray light magnitude is about twice the value in Band 11 compared to Band 10. Figure 6.5 shows the emissivity error distribution using the stray light from TIRS-1. Comparing this to Figure 6.2 it is clear that the resulting LST error is significantly higher than that or TIRS-2, and that there is a significant range in the errors, from -1 K to +0.70 K.

6.5 Comparing 13 Degree and 22 Degree Scatter

In this section, the 13 degree stray light peak will be investigated, which has stray light coefficients of 0.2 % in both of the bands. One would expect that the impact would be less due to the total stray light being less, but I found that this is not the case. Figure 6.6 shows the 13 degree equivalent of Figure 6.1. Comparing the two figures, it is obvious that the 13 degree peak has a higher impact on the LST than the 22 degree. The reason for this is not obvious at first, but looking back at the split window sensitivity analysis from Section 4.2, we see that this is explainable based on the nature of the split window algorithm itself.
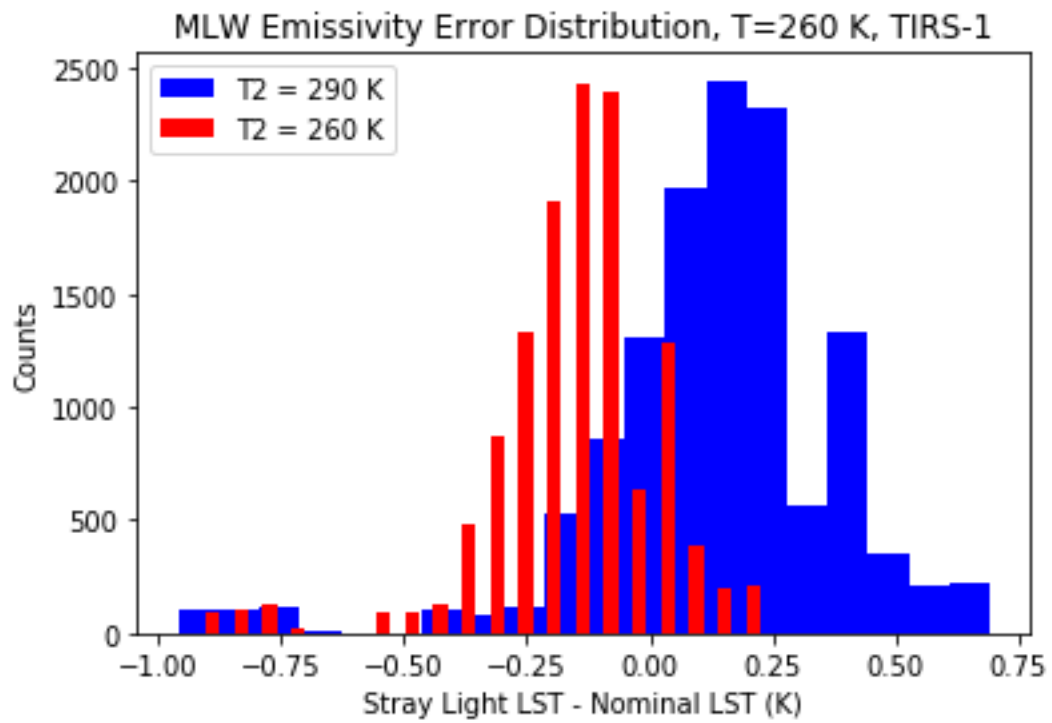
Figure 6.5: Histogram of errors due to in field and out of field emissivity combinations for Landsat 8 TIRS-1. This plot uses the MLW atmosphere with an in-field temperature of 260 K and out-of-field of 260 K and 290 K.
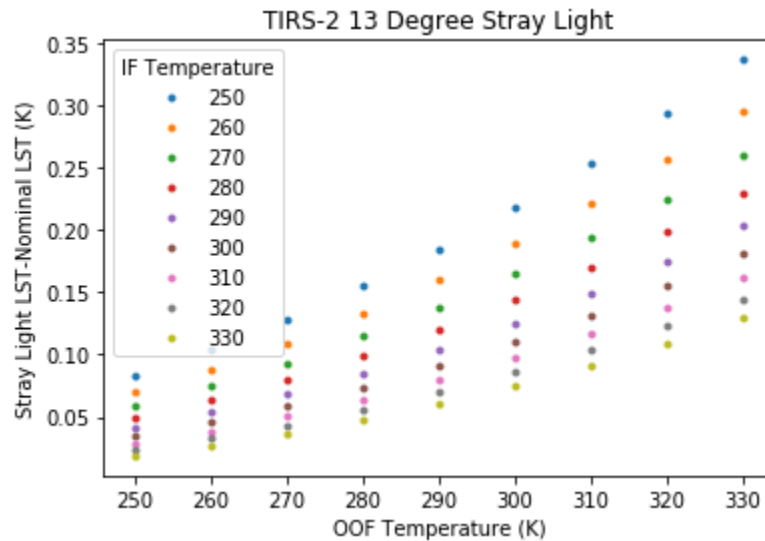
Figure 6.6: This figure shows the preliminary results, similar to figure 6.1 shown in Section 6.1, for the 13 degree scatter for the MLW atmosphere.

Figure 6.9 (a) shows where the 13 and 22 degree scatter coefficients for TIRS-2 fall on the error map, and it is clear that the 13 degree scatter is farther away from the Zero error line, thus having a higher error. Figure 6.9 (b) shows the location of the TIRS-1 coefficients on the error map, which explains why the error is negative. These figures show that the relationship of the stray light of the two bands is more important than just the magnitude of the stray light. This is counter-intuitive at first, but can be explained by understanding how the Split Window algorithm works.
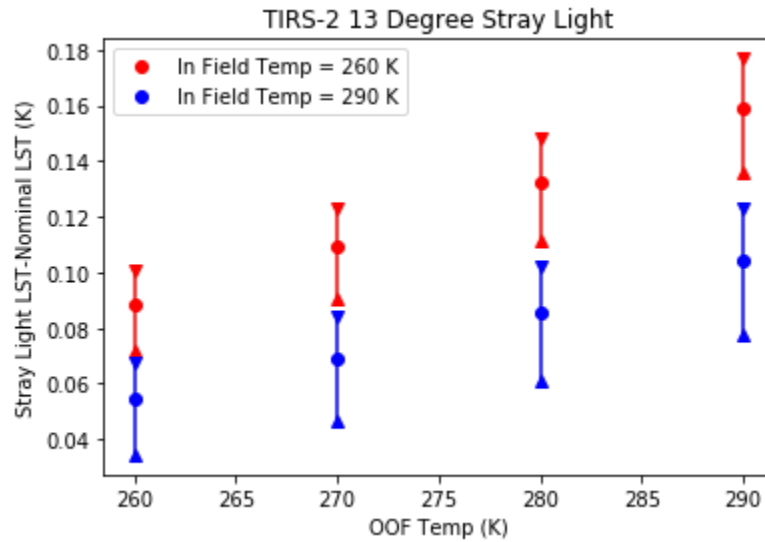
Figure 6.7: This figure shows the preliminary results, similar to figure 6.1 shown in Section 6.1, for the 13 degree scatter for the MLW atmosphere.

(a)

(b)
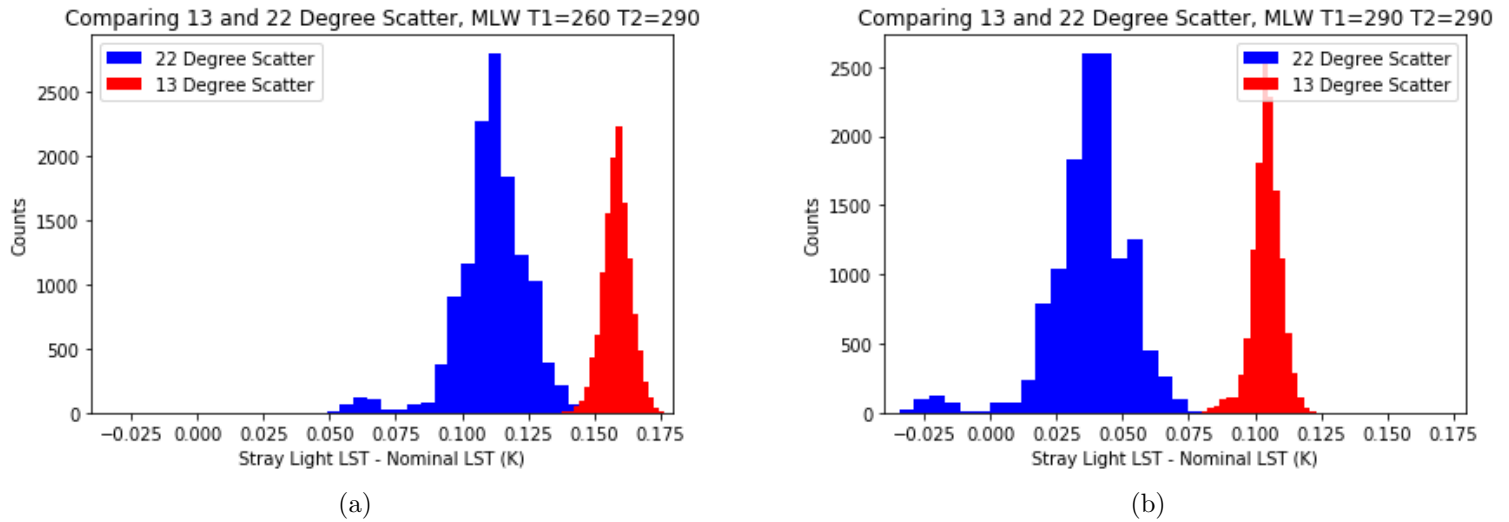
Figure 6.8: This figure compares the LST error distributions due to emissivity for the 13 and 22 degree scatter. In each plot, the in-field temperature is 260 K, and the atmosphere is the MLW. For (a) the out-of-field temperature is 260 K, and 290 K in (b).
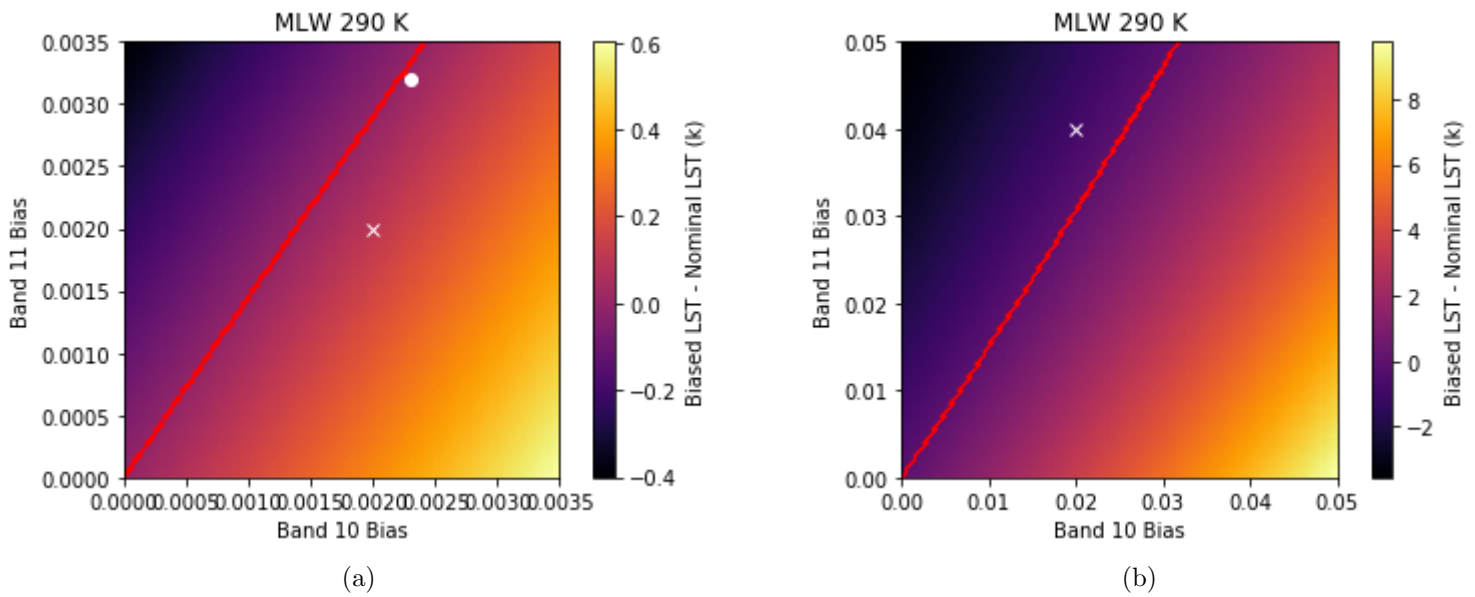
Figure 6.9: This figure shows the location of Landsat stray light coefficients for both TIRS and TIRS-2. (a) Shows the location of the TIRS stray light on the error map with a white X. (b) Shows the location of the 13 Degree and 22 degree scatter peaks, using a white X and a white O respectively.

6.6 Comparing Stray Light to Ground Truth Error

As shown in Chapter 4, the Split Window Algorithm has relatively large errors associated with it as compared to the other studies conducted here. This is important to consider when looking at the impact of stray light. The difference between the predicted LST with and without stray light shows the impact of stray light on the estimated LST, but how these LST values compare to the actual ground truth give more of a practical result, as this is what will effect higher level products that use the Split Window Algorithm. This will help give an idea as to whether or not the stray light will have an impact on the LST product.

Figure 6.10 shows the comparison of the stray light error to the ground truth error. Figures 6.10 (a) and (b) show the emissivity error distribution for the 22 and 13 degree scatter (as seen in Figure 6.8 (a)) respectively. In other words, the blue histogram shows $|LST_{Nominal} - LST_{ground}|$ and the red histogram shows $|LST_{StrayLight} - LST_{Nominal}|$.

Comparing the distributions, it is clear that the stray light error is much smaller than the ground truth error, so this supports the idea that stray light will not have an impact on the LST. It should be noted that this is for a single example, but this example has the largest stray light impact of the five standard atmospheres, as seen above in Section 6.3.

To further express this point, Figures 6.10 (c) and (d) compare the ground truth error with and without the stray light added. In other words,
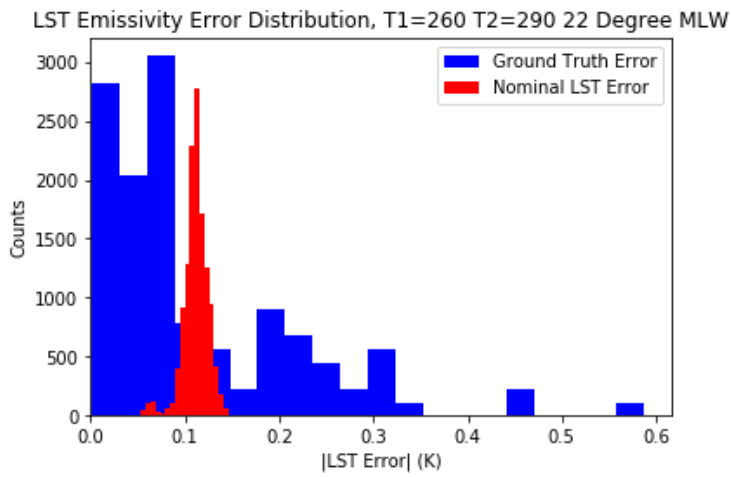
(a) 22 Degree
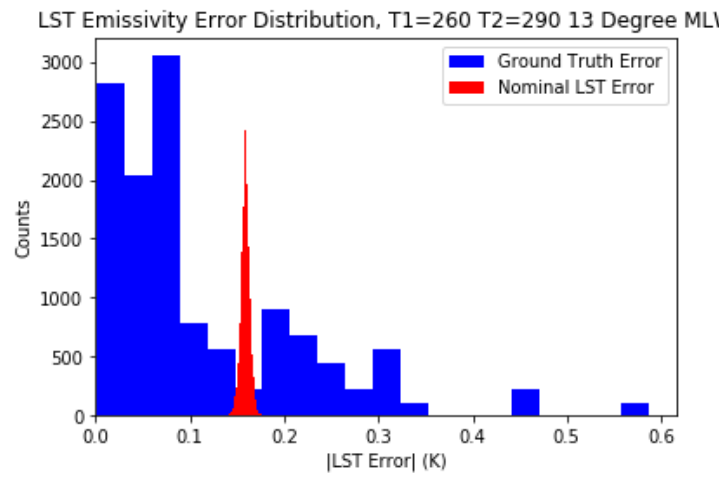
(b) 13 Degree
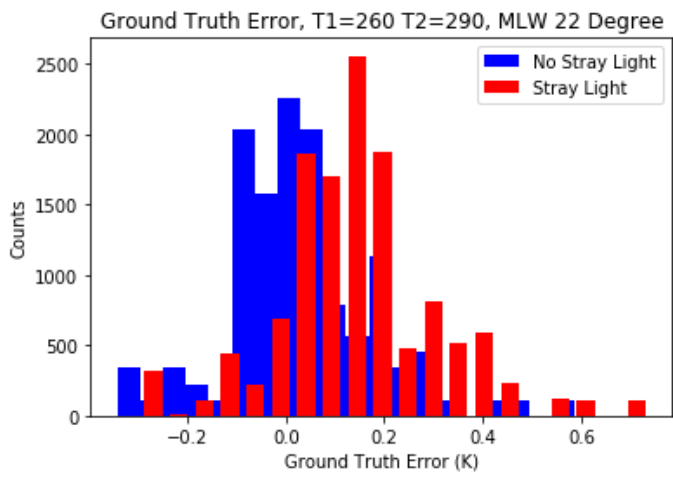
(c) 22 Degree
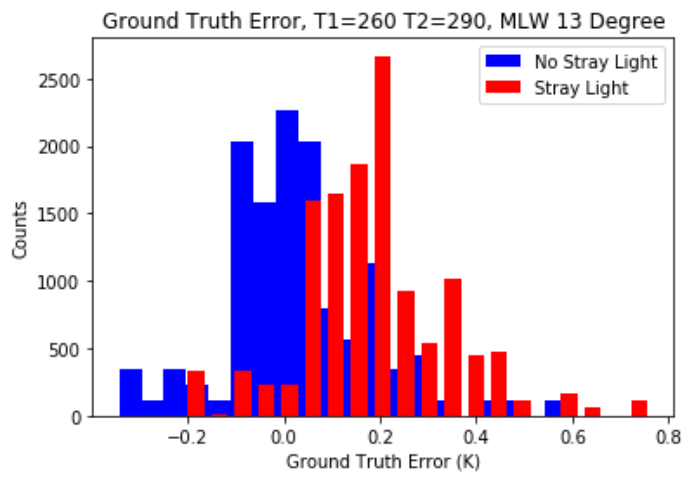
(d) 13 Degree

Figure 6.10
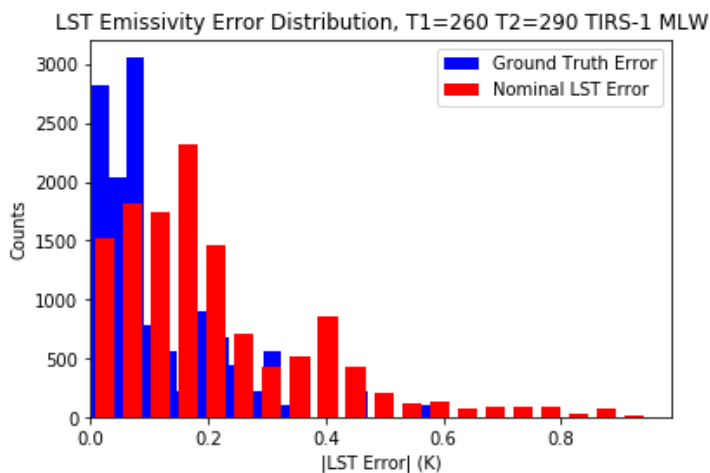
(a) Stray Light vs. Ground Truth
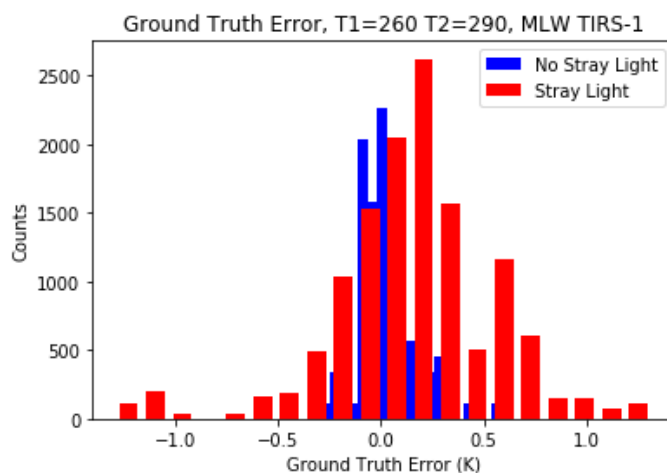
(b) Stray Light vs. No Stray Light

Figure 6.11

the blue histogram shows $LST_{Nominal} - LST_{ground}$ and the red histogram shows $LST_{StrayLight} - LST_{ground}$. There is a noticeable difference between these two distributions, however most of these LST errors with the stray light are still below 0.4 K. In order to get an idea of how small these errors are, these results can be compared to TIRS-1. Figure 6.11 shows the same results as Figure 6.10 with the stray light from TIRS-1. Figure 6.11 (a) shows that the LST error due to stray light is very large compared to the ground truth error, and Figure 6.11 (b) shows that the ground truth error with the stray light is much larger than without the stray light.

6.7 Single Channel and Stray Light Results

All of the previous results were using the Split Window Algorithm, but the Single Channel Method should also be considered as it is also commonly used to calculate LST using TIRS-1. Since the Single Channel Method uses only one band, there will be different LST products for each of the TIRS bands.

6.7.1 TIRS-2 22 Degree Scatter

Figures 6.12 (a) and (b) shows the results of the 22 degree scattering for the single channel method using the two TIRS-1 bands. Comparing this to Figures 6.3, it is obvious that the stray light has a larger impact on the Single Channel Method than the Split Window Algorithm. The Band 11 LST has noticeably higher error in the LST compared to Band 10, where each point in Band 11 is about 1.5 times that in Band 10. This makes sense, since the stray light coefficient for Band 11 (0.0032) is about 1.5 times that of Band 10 (0.0024).

6.7.2 TIRS-2 13 Degree Scatter

Figures 6.12 (c) and (d) show the results for the 13 degree scatter, which is comparable to figure 6.7. In this case, the LST error is lower for the Single Channel Method. This makes sense when thinking about how the Single Channel Method works compared to the Split Window. As stated earlier in Section 6.5, the total stray light is less in the 13 degree scatter, which means

there is less extra signal in the bands, which would not have as much of an impact on LST. This means that the Single Channel Method will behave as expected, unlike the Split Window Algorithm. It also makes sense that the LST error is approximately the same in each of the bands.

6.7.3 TIRS-1 Stray Light

The impact of stray light for TIRS-1 will be replicated using the Single Channel Method, to compare it to the Split Window results. As shown in Section 6.4, the stray light magnitude is significantly larger for TIRS-1 than TIRS-2, by about a factor of 10. In Figure 6.13 we can see the impact that this can have on the LST when using the Single Channel Method. The LST error using this method is significantly larger than using the Split Window Algorithm. One possible explanation for this is that the Split Window Algorithm does not have a simple response to changes in the radiance, as seen in Figure 4.5. Figure 6.9 specifically shows where the TIRS-1 coefficients fall in the Split Window sensitivity plot (for a single example), and it is not far from the area where the resulting LST error is zero. Having two bands also adds more information to the measurements, so it makes sense that it would be less sensitive to error.
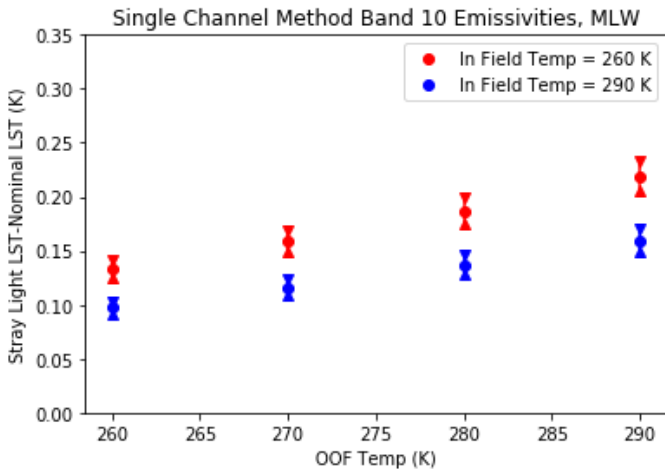
(a) Band 10 22 Degree
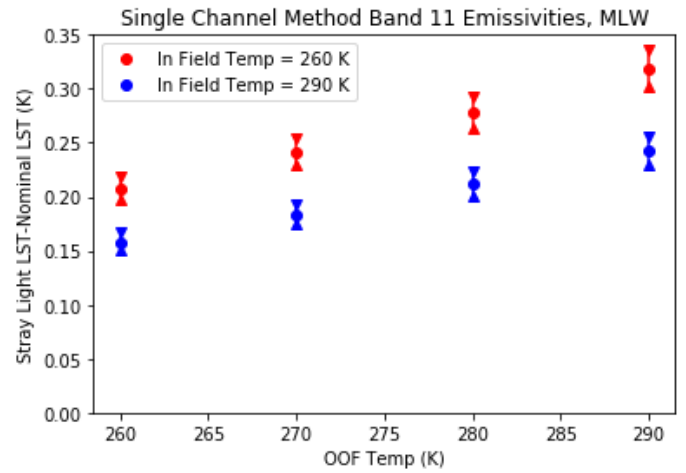
(b) Band 11 22 Degree
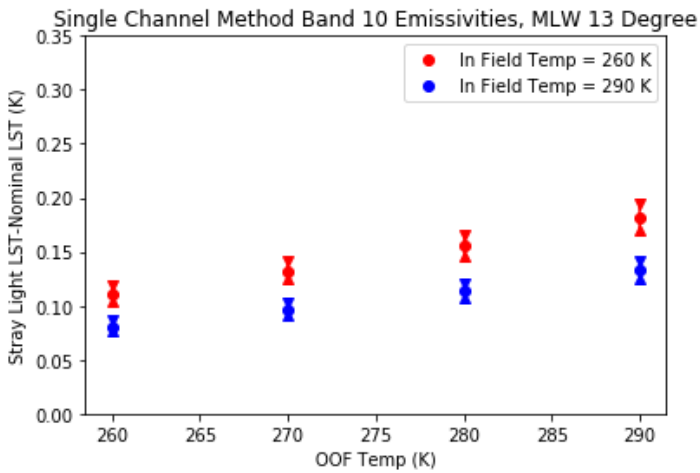
(c) Band 10 13 Degree
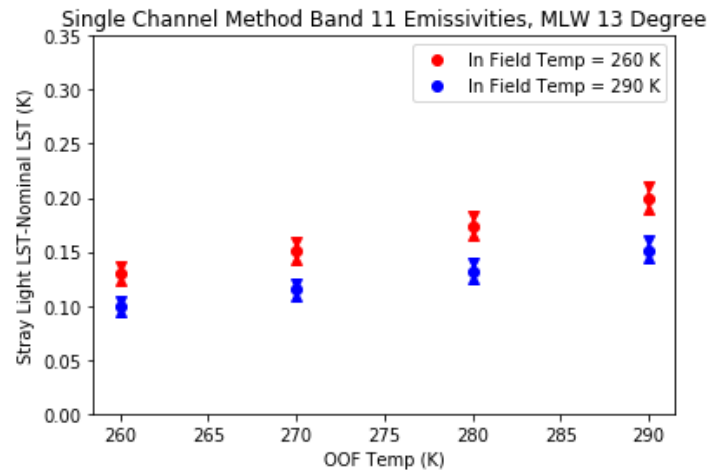
(d) Band 11 13 Degree

Figure 6.12: This figure shows the emissivity stray light result for the Single Channel Method using the TIRS-2 stray light coefficients. (a) and (b) show the results for the 22 degree scatter for Band 10 and 11 respectively. (c) and (d) show the 13 degree results for Band 10 and 11.
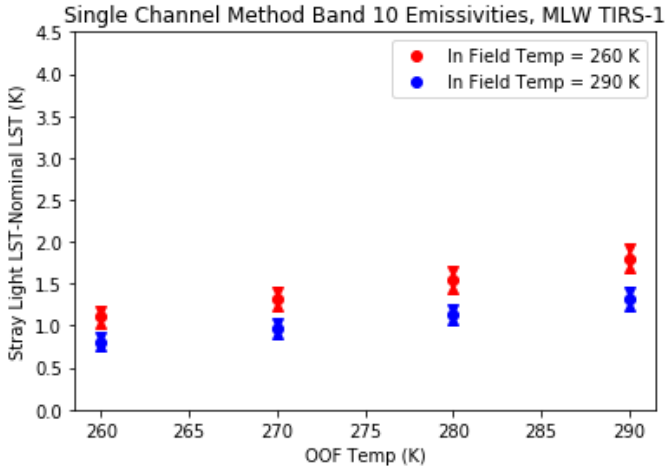
(a) Band 10 TIRS-1
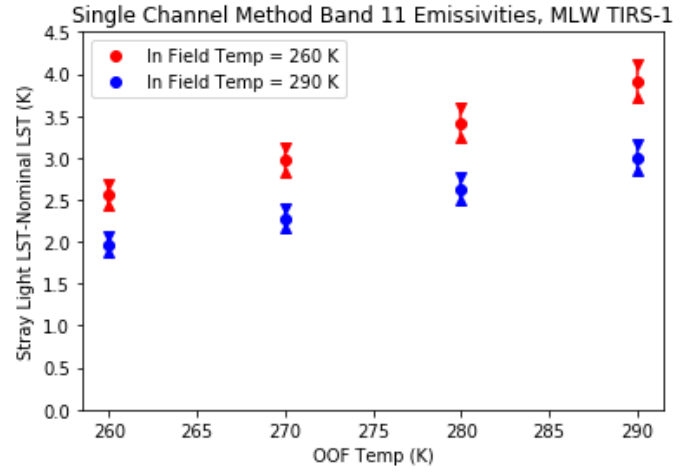
(b) Band 11 TIRS-1

Figure 6.13: This figure shows the range of LST errors due to stray light and different emissivity and temperature combinations for the TIRS-1 Bands.

6.8 Stray Light Summary

In general, the stray light expected from TIRS-2 will be smaller than the required NEdT when using the split window algorithm to retrieve LST. While there is potential for the error to be noticeable, it will most likely not significantly effect the results, and it will be much lower than the residual error associated with the split window algorithm.

For the Single Channel Method, the LST error due to stray light will be larger than the Split Window Algorithm for nearly every case, but it will still be less than the NEdT.

In general, it seems safe to say that the stray light on TIRS-2 will not have a significant effect on the retrieved surface temperature.

Chapter 7

Conclusion and Summary

Thermal remote sensing is a critical source of information for many different fields, and the Landsat satellites have been one of the largest sources of thermal data, and contains one of the longest running archives of thermal data. Landsat-8 saw the introduction of the first thermal instrument with two bands, and this will be continued for TIRS-2 on Landsat 9. This allows LST to be calculated with the Split Window Algorithm using Landsat thermal instruments for the first time, which has advantages over the Single Channel Method which was used for past Landsat thermal instruments.

In this paper, the impact that several different parameters and sources of error can have on estimated LST have been explored in order to help inform the requirements for future thermal instruments. Preliminary work was done on characterizing the Split Window Algorithm, such as calculating the coefficients used to calculate the LST, characterizing the accuracy of the algorithm, and testing how sensitive it is to sources of error such as uncertainty and bias in the measured signal. These studies help set a baseline to compare the LST error in other studies to, and to help understand the results of the rest of the studies in this paper.

The bands study was able to give a rough idea as to how much uncertainty in the bands is needed to introduce more LST error than uncertainty in the measured radiance. For the center of the bands, it was found that a shift of about +/- 50 nm will cause the RMS difference between the nominal and altered LST to be greater than the LST uncertainty due to the measured radiance.

The band shape study has shown that the shape and position of Band 11 seems to be the most important factor when it comes to the accuracy of measuring LST. It also shows that Gaussian bands would have lower error than the nominal bands when altered, but rectangular bands would be as sensitive as the nominal bands. When altering the shape of the bands to make them closer to a Gaussian or rectangular band, there seems to be not much impact on the retrieved LST.

The stray light study has shown that even for some of the most extreme cases, where the out-of-field is 30 K warmer than the in-field, the LST calculated with either the Split Window Algorithm or the Single Channel Method will be less than 0.2 K off from the nominal retrieved LST. The only exception that was found is for the Single Channel Method for Band 11 at the 22 degree scatter, where LST errors can range between 0.15 K and 0.35 K, depending on the in-field and out-of-field temperature. Including different emissivities into this study showed that the emissivity of the targets can be a significant factor, but the maximum difference in LST was still small compared to the expected

84

LST uncertainty due to uncertainty in the measured radiance. Another interesting observation was how the total amount of stray light was not the only factor effecting the LST accuracy, but the ratio of the amount in each of the bands also played in important role. For the 13 degree scatter, the magnitude of the stray light was 0.2 % in each band, and for the 22 degree scatter it was 0.24 % in Band 10 and 0.32 % in Band 11. Even though it had less stray light, the 13 degree scatter had more LST error than the 22 degree scatter. These results make sense when looking at Figure 4.5 in Section 4.2.

Overall these studies have helped shed light on the possible impact of various parameters, and could be used to help inform requirements for future landsat thermal instruments.

Bibliography

[1] J. Schott, *Remote Sensing: The Imaging Chain Approach.* Oxford University Press, 2007.

[2] D. Reuter, C. Richardson, F. Pellerano, J. Irons, R. Allen, M. Anderson, M. Jhabvala, A. Lunsford, M. Montanaro, R. Smith, *et al.*, "The thermal infrared sensor (tirs) on landsat 8: Design overview and pre-launch characterization," *Remote Sensing*, vol. 7, no. 1, pp. 1135–1153, 2015.

[3] F. Jiang, *Evaluation of Stray Light Correction for the Thermal Infrared Sensor (TIRS) from Landsat 8.* Rochester Institute of Technology, 2017.

[4] M. Montanaro, A. Gerace, A. Lunsford, and D. Reuter, "Stray light artifacts in imagery from the landsat 8 thermal infrared sensor," *Remote Sensing*, vol. 6, no. 11, pp. 10435–10456, 2014.

[5] J. C. Lansing and R. W. Cline, "The four-and five-band multispectral scanners for landsat," *Optical Engineering*, vol. 14, no. 4, p. 144312, 1975.

[6] D. P. Roy, M. A. Wulder, T. R. Loveland, C. Woodcock, R. G. Allen, M. C. Anderson, D. Helder, J. R. Irons, D. M. Johnson, R. Kennedy, *et al.*, "Landsat-8: Science and product vision for terrestrial global change research," *Remote sensing of Environment*, vol. 145, pp. 154–172, 2014.

[7] J. H. Hair, D. C. Reuter, S. L. Tonn, J. McCorkel, A. A. Simon, M. Djam, D. Alexander, K. Ballou, R. Barclay, P. Coulter, *et al.*, "Landsat 9 thermal infrared sensor 2 architecture and design," in *IGARSS 2018-2018 IEEE International Geoscience and Remote Sensing Symposium*, pp. 8841–8844, IEEE, 2018.

[8] J. R. Irons, J. L. Dwyer, and J. A. Barsi, "The next landsat satellite: The landsat data continuity mission," *Remote Sensing of Environment*, vol. 122, pp. 11–21, 2012.

[9] A. Pearlman, J. McCorkel, M. Montanaro, B. Efremova, B. Wenny, A. Lunsford, A. Simon, J. Hair, and D. Reuter, "Landsat 9 thermal infrared sensor 2 pre-launch characterization: initial imaging and spectral performance results," in *Earth Observing Systems XXIII*, vol. 10764, p. 1076406, International Society for Optics and Photonics, 2018.

[10] K. A. Semmens, M. C. Anderson, W. P. Kustas, F. Gao, J. G. Alfieri, L. McKee, J. H. Prueger, C. R. Hain, C. Cammalleri, Y. Yang, *et al.*, "Monitoring daily evapotranspiration over two california vineyards using landsat 8 in a multi-sensor data fusion approach," *Remote Sensing of Environment*, vol. 185, pp. 155–170, 2016.

[11] N. Torbick, D. Chowdhury, W. Salas, and J. Qi, "Monitoring rice agriculture across myanmar using time series sentinel-1 assisted by landsat-8 and palsar-2," *Remote Sensing*, vol. 9, no. 2, p. 119, 2017.

[12] Z. Qin, G. Dall'Olmo, A. Karnieli, and P. Berliner, "Derivation of split window algorithm and its sensitivity analysis for retrieving land surface temperature from noaa-advanced very high resolution radiometer data," *Journal of Geophysical Research: Atmospheres*, vol. 106, no. D19, pp. 22655–22670, 2001.

[13] Z. Wan and J. Dozier, "A generalized split-window algorithm for retrieving land-surface temperature from space," *IEEE Transactions on geoscience and remote sensing*, vol. 34, no. 4, pp. 892–905, 1996.

[14] C. Du, H. Ren, Q. Qin, J. Meng, and S. Zhao, "A practical split-window algorithm for estimating land surface temperature from landsat 8 data," *Remote Sensing*, vol. 7, no. 1, pp. 647–665, 2015.

[15] M. Rienecker, M. Suarez, R. Gelaro, R. Todling, J. Bacmeister, and E. Liu, "Merra: Nasa's modern-era retrospective analysis for research and applications," *Journal of Climate*, vol. 24, p. 14.

[16] X. Yu, X. Guo, and Z. Wu, "Land surface temperature retrieval from landsat 8 tirscomparison between radiative transfer equation-based method, split window algorithm and single channel method," *Remote Sensing*, vol. 6, no. 10, pp. 9829–9852, 2014.

[17] M. Montanaro, R. Levy, and B. Markham, "On-orbit radiometric performance of the landsat 8 thermal infrared sensor," *Remote Sensing*, vol. 6, no. 12, pp. 11753–11769, 2014.

[18] B. L. Markham, J. L. Barker, E. Kaita, and I. Gorin, "Landsat-7 enhanced thematic mapper plus: radiometric calibration and prelaunch performance," in *Sensors, Systems, and Next-Generation Satellites*, vol. 3221, pp. 170–179, International Society for Optics and Photonics, 1997.

[19] A. Chedin, N. Scott, C. Wahiche, and P. Moulinier, "The improved initialization inversion method: A high resolution physical method for temperature retrievals from satellites of the tiros-n series," *Journal of climate and applied meteorology*, vol. 24, no. 2, pp. 128–143, 1985.

[20] V. Achard, *Trois problemes clés de lanalyse tridimensionelle de la structure thermodynamique de latmosphere par satellite: Mesure du contenu en ozone, classification des masses dair, modélisation hyper-rapide du transfert radiatif.* PhD thesis, Ph. D. thesis, Univ. Pierre et Marie Curie (Paris VI), Paris, 1991.

[21] F. Chevallier, F. Chéruy, N. Scott, and A. Chédin, "A neural network approach for a fast and accurate computation of a longwave radiative budget," *Journal of Applied Meteorology*, vol. 37, no. 11, pp. 1385–1397, 1998.

[22] A. M. Baldridge, S. Hook, C. Grove, and G. Rivera, "The aster spectral library version 2.0," *Remote Sensing of Environment*, vol. 113, no. 4, pp. 711–715, 2009.

[23] M. Montanaro, J. McCorkel, J. Tveekrem, J. Stauder, A. Lunsford, E. Mentzell, J. Hair, and D. Reuter, "Landsat 9 thermal infrared sensor 2 preliminary stray light assessment," in *IGARSS 2018-2018 IEEE International Geoscience and Remote Sensing Symposium*, pp. 8853–8856, IEEE, 2018.

[24] J. Barsi, J. Schott, S. Hook, N. Raqueno, B. Markham, and R. Radocinski, "Landsat-8 thermal infrared sensor (tirs) vicarious radiometric calibration," *Remote Sensing*, vol. 6, no. 11, pp. 11607–11626, 2014.

[25] J. H. Hair, D. C. Reuter, S. L. Tonn, J. McCorkel, A. A. Simon, M. Djam, D. Alexander, K. Ballou, R. Barclay, P. Coulter, *et al.*, "Landsat 9 thermal infrared sensor 2 architecture and design," in *IGARSS 2018-2018 IEEE International Geoscience and Remote Sensing Symposium*, pp. 8841–8844, IEEE, 2018.

[26] X. Meng, H. Li, Y. Du, Q. Liu, J. Zhu, and L. Sun, "Retrieving land surface temperature from landsat 8 tirs data using rttov and aster ged," in *2016 IEEE International Geoscience and Remote Sensing Symposium (IGARSS)*, pp. 4302–4305, IEEE, 2016.

[27] G. C. Hulley, S. J. Hook, E. Abbott, N. Malakar, T. Islam, and M. Abrams, "The aster global emissivity dataset (aster ged): Mapping earth's emissivity at 100 meter spatial scale," *Geophysical Research Letters*, vol. 42, no. 19, pp. 7966–7976, 2015.

[28] Y. Yamaguchi, A. B. Kahle, H. Tsu, T. Kawakami, and M. Pniel, "Overview of advanced spaceborne thermal emission and reflection radiometer (aster)," *IEEE Transactions on geoscience and remote sensing*, vol. 36, no. 4, pp. 1062–1071, 1998.

[29] S. K. Meerdink, S. J. Hook, D. A. Roberts, and E. A. Abbott, "The ecostress spectral library version 1.0," *Remote Sensing of Environment*, vol. 230, p. 111196, 2019.

[30] J. Cristóbal, J. Jiménez-Muñoz, A. Prakash, C. Mattar, D. Skoković, and J. Sobrino, "An improved single-channel method to retrieve land surface temperature from the landsat-8 thermal band," *Remote Sensing*, vol. 10, no. 3, p. 431, 2018.

Vita

Nicholas Bitten was born in Buffalo, NY.

Permanent address: Hamburg, NY

This thesis was typeset with LaTeX[†] by the author.

[†]LaTeX is a document preparation system developed by Leslie Lamport as a special version of Donald Knuth's TeX Program.